International Journal of Heat and Mass Transfer

Pressure Drop and Heat Transfer Characteristics of Nitrate Salt and Supercritical CO_2 in a Diffusion-Bonded Heat Exchanger

Shaun R. Aakre [a*], Mark H. Anderson [a]

[a] *Department of Mechanical Engineering, University of Wisconsin – Madison, 1500 Engineering Drive, Madison, WI 53706, United States*

Abstract

A lab-scale 316/L stainless steel diffusion-bonded heat exchanger was examined within a coupled high-temperature test facility consisting of an atmospheric-pressure nitrate salt loop and a supercritical carbon dioxide (sCO_2) loop operating between 10-16 MPa. Pressure loss measurements collected for flow rates up to 0.55 kg/s of Solar Salt and up to 0.6 kg/s of carbon dioxide were used to generate friction factor correlations for the respective circular and semicircular zig-zag flow passages. Heat transfer measurements were also performed over a wide range of conditions to produce Nusselt correlations for the CO_2 and nitrate salt side geometries. The Nusselt number is deduced from a heat transfer resistance network and overall conductance measurements collected across the operating envelope of the coupled sCO_2 – nitrate salt test facility. The CO_2 side correlation showed excellent agreement with existing correlations in the literature. The salt side, having nearly circular channels, a different zig-zag angle, and hydraulic diameter, yielded a new correlation applicable to the laminar flow regime. To examine the similitude of the friction correlations, pressure drop testing with water was performed on both sides of the component as well. Finally, results from non-destructive examination are discussed to provide insights regarding inspection methods and draining performance of high-temperature liquids in compact heat exchangers.

Keywords: Diffusion-bonded heat exchanger, zig-zag microchannels, Molten Salt Reactor (MSR), concentrated solar power, thermal energy storage

Nomenclature

Dimensional parameters

C_P	constant pressure specific heat capacity
C_R	heat exchanger capacitance ratio
ΔP	pressure drop across component
G	mass flux
$\bar{h}$	average heat transfer coefficient
$LMTD$	log-mean temperature difference
N	number of microchannels per fluid
Q	heat transfer rate
T	temperature
UA	Overall heat exchanger conductance
$\dot{V}$	volumetric flow rate
ρ, μ, k	fluid density, dynamic viscosity, conductivity

Geometric parameters

a, b	elliptical channel major/minor axis
A_C	core flow area
$A_{s,C}$	cold-side heat transfer area
$A_{s,H}$	hot-side heat transfer area
A_w	wall conduction area
D_h	hydraulic diameter
L_{ZZ}	zig-zag channel length
L_{HT}	core heat transfer length
S	wetted microchannel perimeter
δ	average conduction length
θ	zig-zag angle

Non-dimensional parameters

f_F	Fanning friction factor
K_c	pressure loss coefficient due to contraction
K_e	pressure loss coefficient due to expansion
j	Colburn heat transfer factor
P^*	Header-region pressure loss ratio
Pr	Prandtl number
Re	Reynolds number
Nu	Nusselt number
σ	header flow area porosity

Acronyms

ASME	American Society of Mechanical Engineers
BPVC	Boiler and Pressure Vessel Code
CT	computed tomography
EDM	electrical discharge machining
DBHE	diffusion-bonded heat exchanger
DOE	United States Department of Energy
IRP	Integrated Research Project
ISO	International Organization of Standardization
NSL	Nitrate (Solar) Salt Loop
PCHE	printed circuit heat exchanger
STHE	shell and tube heat exchanger
THL	Thermal Hydraulics Laboratory
VPE	Vacuum Process Engineering
UWM	University of Wisconsin – Madison
$WisCO_2$	Wisconsin Supercritical CO_2 (loop)

1. Introduction

Developers of concentrated solar power and advanced nuclear plants are continually seeking new methods to enhance thermal efficiencies while reducing capital costs. The use of molten salts as thermal energy storage media for concentrated solar or load-following nuclear plants provides opportunities to shift electricity generation from mid-day to the early morning and evening hours when electricity demand and real-time prices are highest. In advanced nuclear plants, the use of molten salt as a primary coolant permits operation at high temperature (> 550°C) while maintaining near-atmospheric pressures in the reactor vessel. These low-pressure reactor vessels and the large volumetric heat capacity of molten salts have potential to significantly reduce plant size, complexity, and capital cost. While low primary-coolant pressures decreases vessel thickness requirements, the primary and intermediate heat exchangers must be constructed of 304 or 316 stainless steel or more expensive nickel-base alloys, such as 800H, 617, 230, or 740H [1] to accommodate high-temperature operation. Traditional shell-and-tube heat exchangers utilized in conventional light-water reactor plants are expected to be exorbitantly large for these advanced salt reactors, leading to excessive salt inventory and heat exchanger material requirements. Several advanced reactor developers are interested in employing the diffusion-bonded heat exchanger (DBHE) to leverage its compactness and reliability at elevated temperatures to decrease the financial risk of these new plants.

Meanwhile, the use of a supercritical working fluids to convert heat stored in liquid salt to electricity is being investigated by solar developers [2]. Supercritical carbon dioxide (sCO_2) is simply CO_2 pressurized above its critical pressure of 7.1 MPa (1080 psi) where separate liquid and gas phases no longer exist, thus boiling or condensation phenomena do not occur. sCO_2 has been proposed to replace or supplement traditional steam cycles for natural gas co-generation, solar, nuclear, geothermal, and industrial waste heat recovery because of its thermodynamic advantages [3]. In addition to higher thermal efficiencies versus Rankine cycles at similar temperatures, prototypic supercritical CO_2 cycles have used compact heat exchangers and smaller turbomachinery to achieve additional capital cost reductions. A compact sCO_2 power conversion unit, potentially a tenth the volume of an equivalent Rankine cycle, is very attractive to developers seeking to employ modular construction methods for rapid, global deployment of low-carbon electricity generation.

The use of DBHEs in the petrochemical industry, its close connection to sCO_2 power cycle development, and growing commercial interest of solar and nuclear system vendors has accelerated the investigation of its thermal performance and mechanical integrity. Aside from uncertainties regarding the thermal hydraulic performance of these heat exchangers, mechanical design rules suitable to DBHE employed in the primary coolant loop of a nuclear reactor do not yet exist. To narrow the gap between the current state of DBHE design and near-term commercial implementation in advanced (Generation IV) nuclear power plants, the U.S. Department of Energy funded an Integrated Research Project (IRP) to investigate its thermal hydraulic and mechanical performance under prototypic nuclear conditions.

The IRP had two main objectives: (1) propose mechanical design, fabrication, and inspection rules for DBHE suitable to Section III, Division 5, Class A of the ASME Boiler and Pressure Vessel Code (BPVC), which addresses safety-related, primary loop components for nuclear reactors operating at high temperatures (>375 – 400°C) and (2) examine the thermal hydraulic performance of commercially available geometries using high-temperatures coolants such as helium, molten salt, liquid sodium, and supercritical CO_2. The first objective was guided by a list of fourteen gaps identified in a draft Code Case for Section III, Division 5, which can be found in [4]. The Code Case gaps were addressed through diffusion-bonded material testing [5], proposal of design rules relevant to Section III [6–8], examination of non-destructive testing [9], and a failure modes and effects analysis.

The second objective was addressed through lab-scale testing of several 316L and 800H DBHE at multiple universities involved with the project [10,11]. This paper focuses on one of these heat exchangers, which to the authors' knowledge, is the first with zig-zag microchannels to be examined under prototypic conditions with nitrate salt and supercritical CO_2. The use of zig-zag microchannels permits the use of existing ASME Section VIII, Division 1 Code rules, which serve as the current mechanical design method for most commercial-scale components. Correlations are proposed for friction factor and Nusselt number for both fluids, and no major operational issues were observed during 200 hours of intermittent operation. The sCO_2 correlations agree with published zig-zag performance data, while the nitrate salt-side correlations show higher friction factor and enhanced heat transfer compared to analytical solutions for straight channels. Discussions of the design, fabrication, and inspection of this heat exchanger are included as these supported the Code Case development by providing context regarding state-of-the-art component design by commercial vendors. Finally, excellent salt draining was observed between five multi-day tests and the component survived a salt freeze-thaw cycle while under a continuous sCO_2 pressure of 10 MPa. The acceptable thermal hydraulic performance and lack of significant operational challenges shows great promise to future developers looking to employ this technology in the near-term.

2. Background

The diffusion-bonded heat exchanger (DBHE), also called a printed-circuit heat exchanger (PCHE) in the literature, is typically composed of plates (~1.5 mm thick) which are photo-chemically etched to create small fluid passages. A major advantage of the DBHE or PCHE is the flexibility of its channel geometry. Unlike traditional shell and tube heat exchangers (STHE) which are restricted to commercially available tube/pipe sizes, a DBHE designer can choose an etched geometry

optimized to the coolant being used. This is especially advantageous for heat exchangers using two drastically different fluids such as supercritical CO_2 and molten salt or liquid sodium. Once the etched plates, or "shims" are completed, the plate geometry chosen for each fluid is stacked alternately. Several unetched plates or "cap sheets" are placed above and below the etched plate stack to provide the required pressure boundary and additional material for attachment of pipe-stub "nozzles", external header shells, and/or structural attachments. Once stacked, some manufacturers may choose to install alignment pins into prefabricated holes in each shim or weld a small bead along the corners of the shim stack to prevent lateral motion between adjacent plates during the bonding process. Next, the unbonded shim stack enters a vacuum furnace equipped with a hydraulic press to apply a compressive load to the stack. Once evacuated and compressed to a prescribed load, the furnace ramps to 1100 - 1300°C depending on the material and the vendor's proprietary bonding conditions. Kept under these conditions for several hours, the crystalline structure diffuses across plate boundaries to form a diffusion-bond.

Extensive experience diffusion-bonding Type 316 stainless steel has resulted in proprietary bonding procedures which possess room-temperature tensile strength and elongation properties consistent with the base material requirements found in ASME, Section II [12]. Collection of high-temperature tensile and creep strength of diffusion-bonded materials is currently being investigated by several vendors, universities, and national laboratories. For ASME Section III, Division 5 applications, only Type 316H and 304H austenitic stainless steels are permitted due to inferior creep resistance of their low-carbon counterparts [13]. Unfortunately, neither of these alloys were readily available in sheet form suitable to diffusion-bonding at the time of the project. The 316/L heat exchanger examined here, could be rapidly manufactured without needing to first qualify the 800H bonding procedure. Despite not being a Section III, Division 5 material, the thermal hydraulic performance and operational context gained from this testing is highly relevant to nuclear applications.

Returning to the thermal hydraulic performance of the DBHE, a plethora of proposed geometries has resulted in a wealth of experimental and numerical studies, many of which are neatly summarized by [14,15]. The most popular geometries include straight or corrugated, 'zig-zag' channels and discontinuous fin geometries which utilize airfoils, staggered rectangular or S-shaped fins to reduce pressure drop without sacrificing thermal performance [16]. Each geometry has its own thermal-mechanical tradeoffs, however the continuous straight or zig-zag channels have been the dominant design in commercially-produced components due to their straight-forward mechanical design procedure and proven durability in the petrochemical industry [15]. Since the component examined here used zig-zag channels for both fluids, the following literature review sections have been constrained to experimental and numerical thermal hydraulic studies addressing supercritical CO_2 and molten salt.

2.1. Studies with carbon dioxide

Carbon dioxide is the most common working fluid employed in DBHE thermal hydraulic studies. This is primarily due to growing commercial interest in the supercritical CO_2 (sCO_2) power cycle. Realizing the improved efficiency of the CO_2 Brayton cycle requires a significant amount of heat recuperation. In the most popular cycle configuration, originally proposed by Feher and investigated further by Dostal, two large recuperators exchange heat between the stream exiting the turbine and the stream exiting one of two compressors [17,18]. To take advantage of low compressibility near the critical point, it is desirable that sCO_2 enters the compressors near 35°C, which leaves 300-450°C of temperature rise to the recuperators. A compact heat exchanger design such as the diffusion-bonded heat exchanger (DBHE) can achieve this temperature rise in a shorter length and potentially at much lower cost, due to its high surface area-to-volume ratio. Given that DBHE provides a great techno-economic option for a sCO_2 power cycle to compete with superheated-steam or ultra-supercritical water cycles, the number of studies in this area has grown significantly in the last fifteen years.

Nikitin examined a 316/L heat exchanger with 37.5° and 40° zig-zags provided by Heatric with sCO_2 near its critical point (2.2 -10 MPa) [19]. Shortly after, Ngo studied a similar component under different flow conditions to propose heat transfer correlations which included Prandtl-dependence in 52° zig-zags [20]. Both these components utilized double-banking on the hot side, meaning two hot plates separated each cold plate. The results were presented in the form of a Nusselt power law relationship, which shows significant enhancement versus the Dittus-Boelter correlation. In 2011, Moisseytev conducted tests at Argonne National Labs on a 316/L PCHE representative of a low-temperature recuperator for a sCO_2 power cycle. Due to limited knowledge of the internal geometry, they generated correlations which include zig-zag angle and pitch as inputs [21]. Around the same time, Kruizenga studied a single etched plate cooled on either side to directly measure the heat transfer coefficient for CO_2 near its critical pressure in straight and zig-zag channels. His results suggested 2.8 and 3.8 times greater heat transfer coefficient in 32.5° and 40° zig-zags compared to straight channels [22]. More recently, Biak performed tests on a diffusion-bonded chiller with 32.5° zig-zag channels on both sides to propose correlations using sCO_2 and water. The experimental results from this study were compared to a CFD study performed by S.G. Kim and found reasonable agreement. Heat transfer performance was adversely affected by CO_2 property non-linearities, while friction factor predictions varied significantly due to assumptions regarding the header and transition regions within the bonded core [23].

Many researchers have used these limited experimental studies to conduct numerical simulations examining the effect of zig-zag angle on pressure drop and heat transfer performance. Lee and Kim utilized experimental results from [19] to optimize the zig-zag angle for a fixed Reynolds number [24]. S.G. Kim used CFD to extend the range of correlations from experimental studies available at the time, up to a channel Reynolds number of 58,000 [25]. This work emphasized the need

for further experimental thermal hydraulic examination of sCO_2 flowing at high velocities in microchannels. Later, Meshram performed simulations to compare zig-zag to straight channels for sCO_2 applications operating within various temperature ranges, representative of the various heat exchangers in a sCO_2 power conversion cycle [26].

Two recent review papers on the thermal hydraulic performance of DBHE express that limited experimental studies have provided useful datasets for validation of numerous computational studies [14,15]. Despite the wealth of studies, the complexity of conducting high-temperature tests with high pressure working fluids has resulted in very little performance data for these components operating at greater than 200°C at the prototypic pressure of 15 MPa or more. As part of the IRP, Katz recently published the performance characteristics of a DBHE operating with helium and supercritical CO_2 [10]. The 316/L component examined in this article utilizes a nearly identical CO_2-side geometry, aside from a slightly longer zig-zag pitch, as the component studied by Katz. This work therefore provides a check of the previous work conducted at Georgia Institute of Technology while operating at higher flow velocities made possible by a larger experimental facility.

2.2. Studies with molten salt

There is very limited experience with molten salt in compact heat exchanger geometries. Despite this, interest in using molten salt as a thermal energy storage media has grown substantially as concentrated solar power and advanced nuclear developers seek to take advantage of its high volumetric heat capacity and stability under ionizing radiation and high heat flux. Most of the fundamental heat transfer studies with molten salt stem from nearly a decade of research conducted as part of the Aircraft Reactor and Molten Salt Reactor experiments performed between 1950 and 1961 [27]. Although fluoride salt mixtures were used as the primary coolant for the experimental thermal-spectrum reactor known as the MSRE, nitrate salts were also used to validate several experimental facilities. Britsch recently summarized several fluoride and nitrate salt heat transfer studies conducted during and since MSRE in [28]. Nitrate salts are generally considered to behave as normal fluids, meaning their heat transfer performance can be predicted by Dittus-Boleter or Seider-Tate correlation [29]. Nitrate salt mixtures melt at lower temperatures (~120 – 280°C) compared to fluorides (~ 450°C) and have been used in industrial applications since the late 1940s [30]. Their high volumetric heat capacity, commercial-scale availability, and low cost has driven their commercial deployment in concentrated solar power facilities with hundreds of megawatt-hours (MWh) of thermal energy storage capacity [31]. Although nitrate salts are not considered a suitable primary coolant for thermal or fast reactors, they are being vetted at an intermediate coolant for sodium-cooled, fluoride salt-cooled, and even helium-cooled reactor concepts by commercial developers in the United States. Intermediate loops are widely considered essential to the safety of advanced salt- or liquid-metal cooled reactors and maintain radioactive primary coolant within the nuclear island. Using nitrate salts in the intermediate loop would leverage their low cost, wide range of operating temperature (250 - 600°C), and decades of industrial experience with molten salt pumps, valves, and steam generators.

While nitrate salts are well understood under turbulent flow conditions, the small hydraulic diameters (~ 0.8 – 2 mm) of DBHE flow passages and the moderate to high viscosity of molten salt results in flows typically within the laminar/transition regime. Analytical solutions for laminar flow in DBHE channels often suggest the convective resistance on the molten salt side would restrict the transfer of heat to CO_2 which is highly turbulent in most DBHE geometries. Therefore, geometry enhancements such as zig-zag channels or staggered fins may be necessary to reduce the convection resistance on the molten salt side and thus reduce overall heat exchanger size. Zig-zag channels disrupt the boundary layer and generate secondary flows within the microchannels which are expected to significantly enhance the convection behavior of the molten salt stream [32].

Assuming nitrate or fluoride salts behave as normal fluids, existing correlations can be used to evaluate the thermal hydraulic practicality of employing these fluids in compact geometries. Kim performed a design study and cost assessment of DBHEs with various geometries for a FLiNaK to sCO_2 application. They determined a respective combination of offset strip fin (OSF) and S-fin passages for the salt and sCO_2 sides to be the most cost-effective design. Acknowledging the difficulties associated with designing and fabricating discontinuous fin geometries, the 52° zig-zag geometry investigated by Ngo [20] was also suggested to be a good CO_2-side geometry selection [33]. Ronco compared a helical coil heat exchanger to a PCHE for a fast-spectrum molten fuel-salt reactor. Heat exchanger compactness is especially important for fuel-salt reactors to limit fissile material outside the critical region. Assuming the analytical solution for friction factor and Nusselt in a straight semi-circular duct, the PCHE was determined to be the optimal choice to reduce financial and technical risk [34]. Wang recently conducted a study of molten salt in a brazed plate heat exchanger which used airfoil fins [35]. This work showed that nitrate salt and heat transfer oils share excellent thermal hydraulic performance in this discontinuous fin geometry, however the structural integrity of these geometries is still under investigation. Since this component was brazed and had small bond coverage area, it is not suitable for prototypic nuclear plant conditions. Fu numerically analyzed a PCHE with sCO_2 in an airfoil-fin geometry while salt operated in the straight, rectangular channels. They found this to be a good configuration but experimental validation is required [36]. Shi performed a numerical analysis on an airfoil-fin heat exchanger using sCO_2 and a chloride salt [37]. The thermal hydraulic results were compared to zig-zag experimental data obtained with helium and water published by Kim and No [38]. Again, airfoils were considered a very attractive option for both the sCO_2 and molten salt sides of the PCHE.

Despite the promising technical and economic implications, there are currently no experimental studies for molten salt operating in conjunction with a high-pressure working fluid in a DBHE designed using BPVC rules. Most proponents of the technology suggest the salt-side hydraulic diameter should be maximized by employing formed plates or thicker etched shims to create larger channels than those typically associated with common DBHE designs. This work serves to address these concerns by utilizing a circular channel geometry on the salt-side which provides a larger hydraulic diameter without using different shim thicknesses for each fluid or employing a "hybrid" design with mechanically formed plate fins. The data presented here shows that nitrate salts can be employed in existing zig-zag geometries with reasonable pressure drop and enhanced heat transfer performance versus analytical predictions for straight channels. Suggestions for future work with molten salt compact heat exchangers are provided in the discussion section to highlight the need for further experimentation.

3. Experimental Method

3.1. Heat Exchanger Description

The diffusion-bonded heat exchanger (DBHE) examined here has external dimensions of 57.4 x 72.6 x 344.4 mm and was constructed of dual-certified 316/L stainless steel 16-gauge sheet (ASME SA-240) by Vacuum Process Engineering (VPE). It has 15 cold CO_2 layers separated by 14 hot nitrate salt layers. The CO_2 channels are semicircular, while the salt channels have a nearly circular cross-section. The circular channel is made possible by stacking two plates with mirrored etch patterns facing one another. The circular channel was specifically requested to reduce plugging concerns, minimize pressure losses, and explore the manufacturability of circular channels on the molten salt side. Semi-circular channels were chosen for the CO_2-side to leverage extensive experience with this geometry. While circular channels could have been employed on the CO_2-side as well, uncertainty associated with the misalignment of mirrored plates and the resultant stress concentration were also considered in this selection.

Figure 1 shows the heat exchanger before and after installation between sCO_2 and nitrate salt loops. The heat exchanger operates in a counterflow configuration with salt flowing upward and sCO_2 flowing downward. Using an upward flow configuration allows all salt-side piping in the experimental section to be slanted upwards. This configuration is chosen to enable reverse-drainage during shutdown. While draining the loop, salt remaining in the test section flows backwards toward the supply tee near the bottom of the Nitrate Salt Loop (NSL). Table 1 includes the design specification for the 316/L DBHE examined by this work. The flow area was sized to achieve at least 0.5 kg/s of salt flow for a 5-psi (35 kPa) pressure drop. A nominal heat transfer rate of ~27 kW was selected to reflect the maximum heat input to the salt inventory. The right image in Figure 1 shows the location of two pairs of CO_2 pressure measurement ports. The taps on the CO_2 supply/return nozzles also contained thermocouples which measured the inlet and outlet CO_2 temperatures. The thermocouple tips were located on the centerline of these nozzles to measure the bulk CO_2 temperature entering/exiting the heat exchanger. Two additional pairs of pressure taps were included for salt-side pressure drop measurement. One pair was on the opposite side of the CO_2 core pressure taps, as shown in the left image of Figure 1. The second pair was located on the supply/return piping near the heat exchanger nozzles. The right image in Figure 1 shows one of two salt pressure transducers connected to the outlet piping, directly above the DBHE. The other transducer was located 30 cm upstream of the inlet nozzle, where there was sufficient room for vertical orientation with respect to the supply line. The salt-side thermocouples were installed in ports protruding from the piping elbows shown in the middle image, such that the thermocouple junction was in the center of the headers. More information on these measurements is provided in the next section.

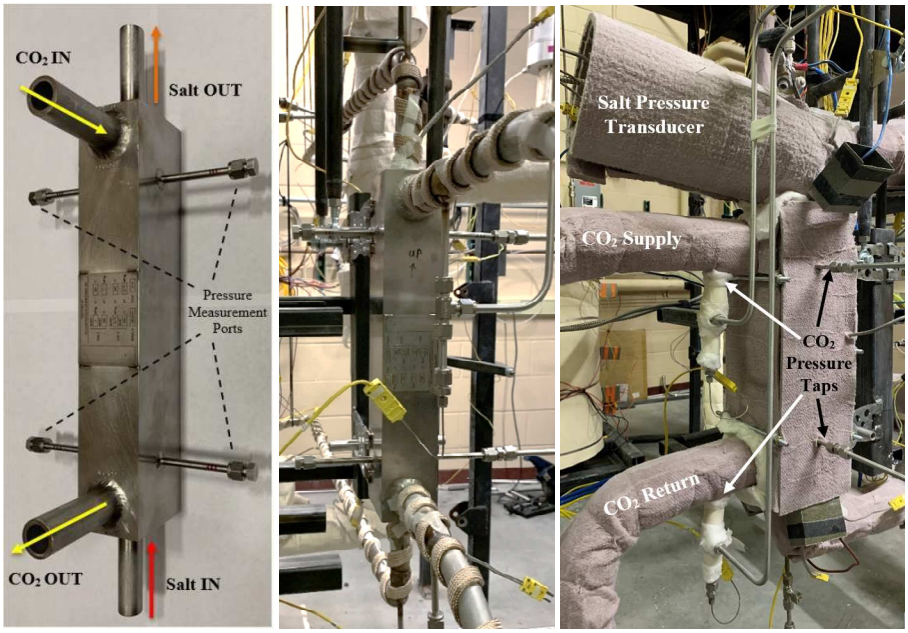

Figure 1. 316 Nitrate Salt – CO2 heat exchanger before installation (left), integrated between loops (middle), and after installation of heaters and insulation (right)

Table 1
Design Point of 316/L Test Heat Exchanger

Parameter	**Hot (Solar Salt)**	**Cold (sCO_2)**
Design Pressure	1 MPa (145 psi)	22.8 MPa (3300 psi)
Design Temperature	560°C (1040°F)	
Nominal Flow Rate	0.35 kg/s	0.16 kg/s
Est. Pressure Drop	*15 kPa (2.2 psi)*	*172 kPa (25 psi)*
Inlet/Outlet Temperature	*500°C* ← 550°C	400°C → *539°C*
Overall HT Coefficient	2275 W/m^2-K	
Heat Duty at Design Point	27 kW	

** Values in italics were predicted by manufacturer*

As mentioned above, the IRP encompassing this work focused on the development of diffusion-bonded heat exchangers for ASME Section III, Division 5 (nuclear applications). Shim materials approved for use in this Code, such as stainless steel 304H, 316H, Inconel 800H or 617 were not readily available in at the beginning of the project. Therefore, a dual-certified 316/L component was ordered to leverage lower cost and improved lead time. While the primary goal was to examine the thermal hydraulic performance of this component, its design, fabrication, and inspection methodology were carefully tracked and summarized here to provide context for future development and testing required to qualify diffusion-bonded heat exchangers for nuclear applications. Although nuclear-grade and some solar-industry DBHEs may be constructed with different materials with enhanced creep-resistance, the thermal hydraulic performance and operational context gained from this testing is highly relevant to high-temperature applications.

Two of the fourteen technical gaps associated with Section III, Division 5 Code Case outlined by [4] relate to non-destructive examination of these components post-fabrication and during in-service inspection. A recent survey of non-destructive examination techniques, including ultrasonic examination, x-ray and neutron radiography for these components was provided by Selby [9]. Before any thermal or hydraulic testing of the heat exchanger was performed, it was examined with a 450-kilovolt x-ray tomography system at University of Wisconsin-Madison. This industrial computed tomography system was purchased to support the Code Case development effort by providing internal imaging capabilities for each heat exchanger before and after testing at high-temperature or after induced rupture by hydrostatic testing. The computed tomography (CT) capabilities of this system provide a means to inspect the etched channels and internal header regions without dissecting the component. The vendor, VPE, has permitted the authors to include the images of the zig-zag core region shown below in Figure 2. These images do not show the internal headers or flow transitions located between the inlet/outlet nozzles and core region to protect the proprietary nature of this region.

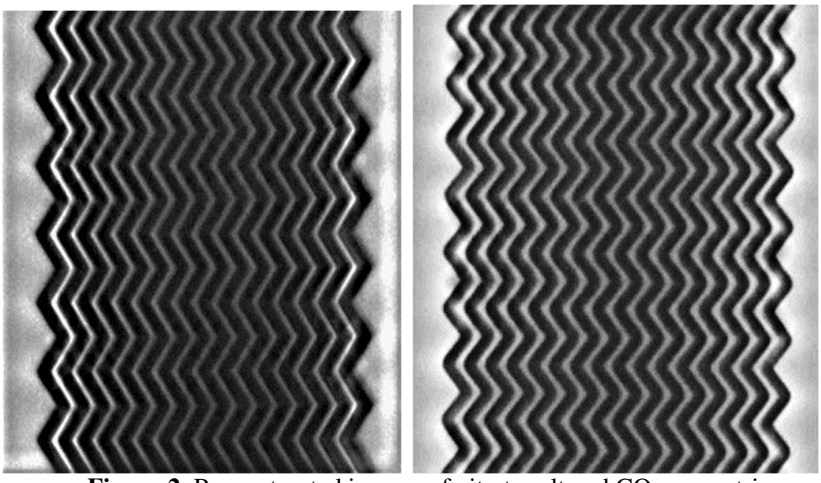

Figure 2. Reconstructed images of nitrate salt and CO_2 geometries

The left-side of the Figure 2 shows the mid-plane of the near-circular nitrate salt channels. Note that the zig-zag angle is less aggressive compared to the CO_2 geometry shown on the right side of Figure 2. The depth of the circular salt channels is limited by the pressure boundary requirement for the adjacent sCO_2 stream; however, their hydraulic diameter is increased significantly due to the near-doubling of the flow area compared to the semi-circular CO_2 channels. Thicker shims could be used on the salt-side to increase the diameter further, but the same 16-gauge shims were used for both etched geometries.

Using a combination of the images obtained from the CT reconstruction and an unbonded shim sample provided by VPE, the channel dimensions in Table 2 were estimated for dimensionless presentation of pressure drop and heat transfer results. The CT scans provided images with a 90 μm resolution, which is near the etch tolerance observed for previous stainless-steel components built for UW-Madison. Experience with 316/L has reduced the etch tolerance to less than 70 μm. This tolerance must be applied to the mechanical design calculation to ensure sufficient wall thickness to contain the pressure within each channel. Smaller tolerances could effectively increase compactness and improve performance by reducing nominal wall thickness required to meet the existing mechanical design criteria found in Section VIII, Division 1, Appendix 13-9 [39].

The existing Section VIII code rules for diffusion-bonded pressure vessels were used to determine the channel dimensions for this component. These rules treat each microchannel as individual rectangular pressure vessels and assume a weld efficiency factor of 0.7 at the diffusion-bonded interface due to the inability to inspect each bond after fabrication. As neatly summarized by [40], the existing rules are restricted to three stainless-steel construction materials, and these components may not be used for "potentially lethal" substances. Therefore, the component examined here is designed according to a proven design methodology, however this design technique has yet to be proven sufficient for abnormal loading conditions associated with design-basis events in a nuclear plant, such as a seismic event or loss of flow accident. Furthermore, Section III, Division 5 requires time-dependent properties for creep and fatigue analysis at high temperatures which limits the allowed construction materials to those which have sufficient long-term creep data [4].

3.2. Heat Exchanger Geometry

Calculation of the hydraulic diameter, flow area, and heat transfer area associated with the zig-zag microchannels requires special attention to the etch profile. This section provides a detailed description of these parameters, as they are crucial to the dimensionless results presented in this paper. Variation in the calculation of hydraulic diameter, core flow area, and heat transfer area has somewhat clouded the literature addressing DBHE geometries. Typically, the etched channel cross-section is designed to be semi-circular from the perspective of the fluid between bends. However, if one were to look down the longitudinal axis of the heat exchanger, the channel cross-section takes the form of a semi-ellipse. This skewed, elliptical channel profile remains nearly constant along the length of the heat exchanger and was first suggested by Baik [23] to be a more accurate representation of the flow area.

Figure 3 shows a generic example of a corrugated "zig-zag" channel which are commonly employed in diffusion-bonded heat exchangers. The shaded half of the microchannel cross-section represents the common semi-circular geometry found in many of the previous studies summarized above. The dashed portion of the cross-section represents the mirrored geometry which creates near-circular channels, like those employed on the salt-side of the heat exchanger discussed here. The 316/L heat exchanger introduced above alternates between one shim for CO_2 and two shims for the salt-side. The view shown on the left of Figure 3 provides a visual example of how the skewed, (semi-) elliptical cross-section results from zig-zag channels with a (semi-) circular profile between bends.

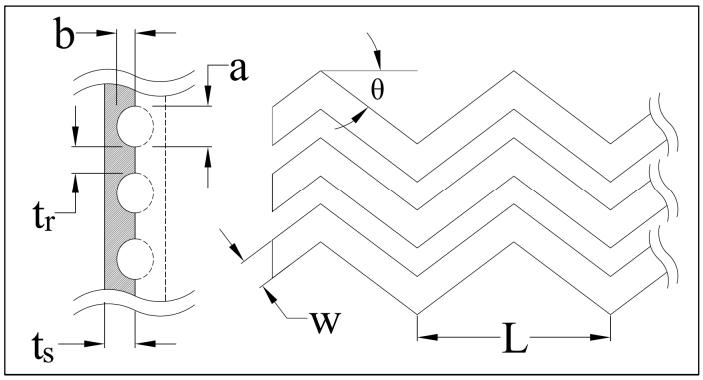

Figure 3. Geometric characteristics of zig-zag microchannel

Since the CO_2 and nitrate salt-side geometries of the heat exchanger have zig-zag channels with semi-elliptical or elliptical cross-sections when viewed macroscopically, the following approach is used to calculate the geometric parameters in Table 2. The hydraulic diameter is calculated using the wetted perimeter and area of the (semi-) elliptical channels. The wetted perimeter (S) of the elliptical salt channel is approximated by equation 1, using the skewed width (a) and the etch depth (b). The etch depth is assumed to be half the etch width (w) since the etch profile from the perspective of the fluid is nearly semi-circular. Because the skew angle is low, and the error associated with this approximate calculation of elliptical perimeter is less than 0.5%. A similar approach was used to for the semi-elliptical channel perimeter, except half the elliptical perimeter was added to the skewed width (a), which is simply the etch width (w) divided by the cosine of the bend angle (θ).

$$S = 2\pi \sqrt{\frac{1}{2}\left[\left(\frac{a}{2}\right)^2 + b^2\right]} \quad \textbf{[1]}$$

The flow area for each microchannel is defined as the skewed (semi-) elliptical area as well. The hydraulic diameter is then calculated as four times the flow area divided by the channel perimeter (S). Finally, the core flow area is defined as the sum of all flow channels multiplied by the microchannel flow area. The combined flow area of all the channels in the core is 6.2 and 2.7 cm^2 for the salt and CO_2 sides, respectively. This unusually large difference in flow areas for a DBHE was made possible by the unique circular channels on the salt-side. Also, one can see how a modest increase in the etch width and the application of a mirrored geometry significantly increases the hydraulic diameter on the (hot) salt-side.

Table 2
Measurements of internal geometry

Parameter		Hot Side (Nitrate Salt)	Cold Side (CO_2)
# of plates		14	15
# of channels - N		224	240
Channel shape		*Circular ZZ*	*Semicircular ZZ*
Etch width - w	[mm]	1.75	1.43
Wavelength	[mm]	9.5	7.2
Bend angle - θ	[°]	30°	37°
Surface Roughness	[μm]	1.8 - 2.2	N/A
Hydraulic diameter - D_h	[mm]	1.87	1.00
Core flow area - A_c	[mm^2]	619	270
ZZ flow length - L_{zz}	[mm]	272	293
HT Surface area - A_s	[m^2]	0.405	0.332
Core HT length - L_{HT}	[mm]	270	
Conduction area - A_w	[m^2]	0.166	
Conduction distance - δ	[mm]	1	
Compactness factor	[m^{-1}]	510	

Calculation of heat transfer area requires some additional assumptions. The flow direction and velocity in the header/distributor region is not the same as in the core. The zig-zag core makes up approximately 270 mm (10.67 inches) between the transition regions located between the header and core. Due to a lack of complete information of the header geometries, the ~ 35 mm of length associated with these regions is assumed to not participate in the heat transfer between

fluids. The assumption that the header regions do not provide a significant contribution to pressure drop or heat transfer performance is common in experimental DBHE studies due to limited information. Using the channel perimeter (S), the number of channels for each fluid (N), and the core heat transfer length (L_{HT}) divided by the cosine of the bend angle (θ), the heat transfer surface area is calculated for each stream using equation 2. The incorporation of the bend angle considers the full flow passage length of the zig-zag channel. A sharper zig-zag angle therefore increases the amount of heat transfer area within a given length of heat exchanger. Some studies do not account for this "total" passage length which has skewed the comparison of heat transfer results in the literature. Using equation 2, the heat transfer (A_S) or wetted surface area for the hot and cold sides to calculated to be 0.405 and 0.332 m^2, respectively. Adding these heat transfer areas together and divided by the core volume yields the compactness factor shown in Table 2.

$$A_S = S \cdot N \cdot L_{HT} / \cos\theta \quad \textbf{[2]}$$

3.3. Heat Exchanger Test Facility

The DBHE testing described here was performed within the Thermal Hydraulics Laboratory (THL) at the University of Wisconsin – Madison. An existing Nitrate Salt Loop (NSL) was coupled to the Wisconsin Supercritical CO_2 (WisCO2) loop by the heat exchanger described above. The NSL is 7.2 m tall and 1.5 m wide and is capable of driving flows of 600 L/min of Solar Salt at up to 600°C. During start-up, all piping and 375 kg of Solar Salt inventory is heated to 300°C via external heaters. Then, 345 kg of the 0.6 $NaNO_3$ – 0.4 KNO_3 (mass fraction) salt is forced through a dip-tube into the bottom of the loop by pressurizing 270 L storage reservoir on the floor. A Nagle cantilevered centrifugal pump is submerged in a 250 L reservoir at the top of the loop. The gas space in the pump reservoir is left open to the atmosphere with lines running to the laboratory's ventilation system. The pump discharge directs salt flow downward through a 3.5-inch Schedule 40 pipe (ID = 77.9 mm) which encloses three 1-inch Schedule 40 pipes (OD = 33.4 mm) in a triangular array. Each inner pipe in the array houses a cartridge heater for a combined heat input near 18 kW. At the end of the downcomer near the bottom corner of the loop, a tee directs some flow toward the heat exchanger. The experimental section consists of a wire-mesh filter, pneumatic isolation valves at the entrance and exit, the heat exchanger, and a venturi flowmeter. The experimental section piping returns to the main loop at a tee downstream of a globe valve which governs the available pressure differential across the test section.

After initial testing, a 50 kW heater rod was installed to enable steady-state operation of the heat exchanger at higher flow rates and heat transfer rates. The NSL is monitored and controlled by a LabVIEW visual interface. The interface includes data acquisition for the temperature measurements and provides control signals to the pump's inverter, trace heat zones, heater cartridge array, and the Stern rod heater. A sample of the salt mixture extracted during testing was examined via inductively coupled plasma mass spectroscopy (ICP-MS) to validate the salt's composition. This technique approximately bounded the salt's mass composition to 59.9 +/- 2.2% $NaNO_3$ and 40.9 +/- 1.5% KNO_3.

The $WisCO_2$ loop was built specifically for high-pressure, high-temperature testing of compact heat exchangers. The loop consists of a triplex positive-displacement pump, buffer volume, pump pre-chiller, a recuperative DBHE, and dedicated high-performance liquid chromatography (HPLC) pump to fill the loop above bottle pressure (> 6.2 MPa). The pump is unique in its ability to compress both liquid and supercritical CO_2 provided the inlet density remains high. Additional details on the pump design and its performance can be found in [41]. For this work, the loop provides CO_2 flow rates up to 0.6 kg/s for the test heat exchanger at pressures up to 16 MPa. While the heat exchanger is designed to 22 MPa at 550° C, the tests presented here were limited to 16 MPa due to limitation of differential pressure and mass flow instrumentation. All salt-side measurements relevant to heat exchanger performance quantification were collected by a separate LabVIEW program controlling the $WisCO_2$ loop. This allowed synchronized measurements of both the nitrate salt and CO_2 instruments discussed below.

Figure 4 shows the $WisCO_2$ loop coupled to the NSL by the SS316/L DBHE. The operating conditions of the heat exchanger is determined by several operator inputs. Flow rates are controlled by the nitrate salt and CO_2 pump speeds and the position of the NSL globe valve and a bypass (needle) valve on the $WisCO_2$ loop. Salt inlet temperature is controlled by the cartridge heater array and the DC-powered Stern rod. CO_2 inlet temperature is governed by the effectiveness of the 800H recuperator. Since the effectiveness of the recuperator remained above 95%, the CO_2 supply was typically less than 50°C below the return temperature. To reduce uncertainty in heat rate cause by low temperature differential across the salt-CO_2 heat exchanger, up to 30% of the cold-side flow was bypassed around the recuperator to reduce the CO_2 inlet temperature. The two pneumatic isolation valves were incorporated into the test section to isolate the heat exchanger from the salt loop during start-up or in the event of a heat exchanger failure. The Coriolis and venturi flow meters are shown along with the approximate location of pressure transducers and thermocouples used to calculate pressure loss and heat transfer rate during testing. More detailes on the use of these measurements and the propagation of their uncertainty into the final results are provided below. Finally, several different wire-mesh filters were employed in the test section to capture particulates in the molten salt stream. A 400-micron mesh captured most particulates in the salt volume with acceptable pressure losses and prevented any plugging or accumulation of particles in the DBHE. A 40-micron wire mesh is only recommended for temporary filtering operations, as this resulted in excessive pressure losses during testing.

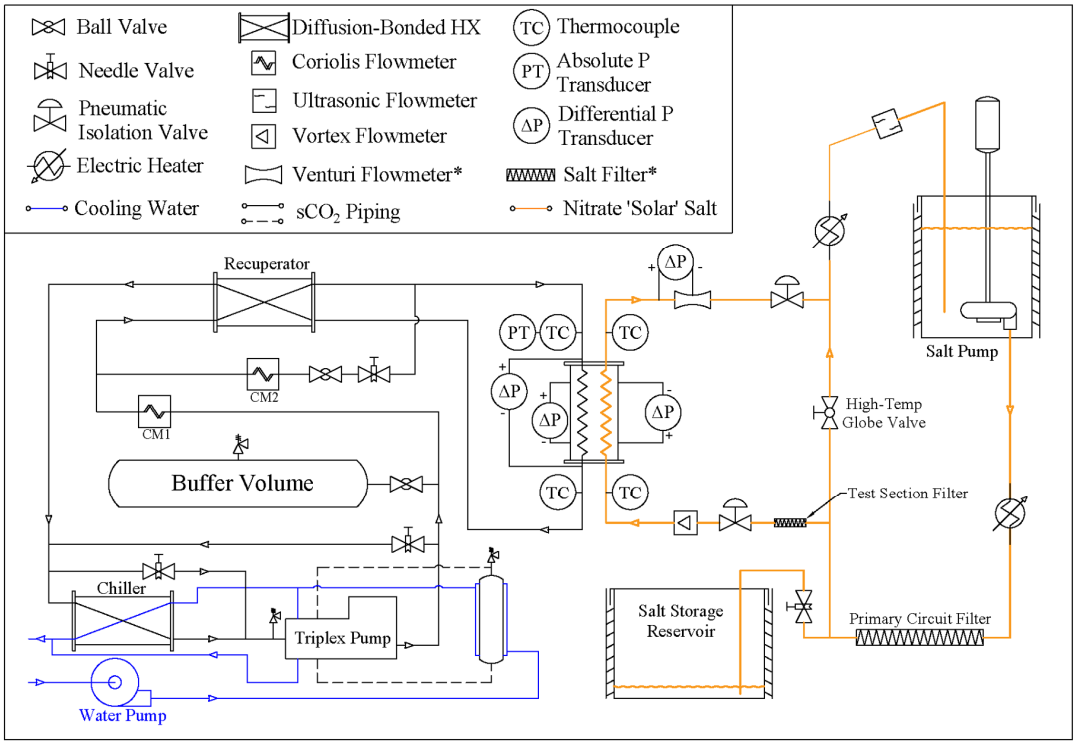

Figure 4. Schematic of WisCO$_2$ loop connected to the NSL

A separate low-pressure water test facility was also used to conduct friction factor testing on the heat exchanger and to examine the venturi flowmeter's performance in water. The loop was equipped with a centrifugal pump controlled by a variable frequency drive. A fan-cooled radiator and bypass circuit allowed for temperature regulation of the water volume and fine flow control through the test section, respectively. The system could be pressurized up to 4.2 barg (60 psig) by applying air pressure to the gas space of a pressurizer connected to the suction pipe to suppress cavitation in the venturi flow meter or heat exchanger at high flow rates. The test section consists of inlet and outlet thermocouples, a Foxboro CFS10 Coriolis flow meter, and two differential pressure transducers, a Siemens SITRANS P and a Yokogawa EJA110E with maximum spans of 1.6 and 5 bar respectively. During venturi testing, only the Yokogawa transducer was used, while both were used for zig-zag friction testing to measure the pressure drop across the core and the entire heat exchanger simultaneously. Results from the venturi test are discussed in Section 3.5, while results from friction factor testing are discussed in Section 4.1 below.

3.4. Instrumentation

Mass flow rate, pressure drop, and terminal temperatures were measured on both sides of the heat exchanger to determine the pressure loss and heat transfer characteristics of each zig-zag geometry. On the CO_2 side, the mass flow was measured by a Coriolis flow meter (MicroMotion F050P) and pressure losses between the core pressure taps and between the nozzles were measured by two differential pressure transducers (Siemens SITRANS P), separated from the heat exchanger by 0.5 m lines for thermal isolation. On the salt side, the flow rate was measured by a venturi flow meter designed and calibrated in-house. The calibration procedure and determination of measurement accuracy for the venturi flowmeter is discussed below. The salt-side pressure drop across the venturi and the heat exchanger were each measured by a pair of Rosemount pressure transducers with remote-sensing diaphragms filled with Silicone 704 oil. Each remote diaphragm was surrounded by thin-walled section of pipe with a trace heater. The trace heater was set to maintain each transducer at a temperature between the salt's melting point of 220°C and the fill-oil's decomposition temperature of 315°C. The quarter-inch tube (ID = 3.8 mm) between the heat exchanger and the pressure transducer acted as a fin to step down the salt temperature from the operating temperature to within the allowable range for the pressure transducers. Since the salt is highly incompressible, the salt flowing through the heat exchanger or venturi transmits its pressure to the salt in the pressure taps and within the diaphragm housing. After filling the loop with salt, each transducer was bled through a port in the top of the diaphragm housing to remove any trapped air. The salt flow was stopped several times a day during testing to record any change in the zero-flow signal. These measurements are used to establish parameters in the uncertainty analysis below. Finally, K-type thermocouple

probes were inserted into the salt-side headers/plenums and at the entrance/exit of the CO_2 header ports for terminal fluid temperature measurement.

3.5. Venturi Flowmeter Validation

The venturi flow meter used to measure the nitrate salt flow rate was designed with guidance from the ISO Specification 5167-4 [42]. Due to the relatively low flow rate in the 13.5 mm diameter salt piping and the salt's viscosity, the Reynolds number is far below the 200,000-minimum required to use the constant-value discharge coefficient in the ISO specification. Although the throat-to-inlet diameter ratio was within the recommended range, the inlet diameter (13.5 mm) was also below the minimum of 50 mm. Reader-Harris has compiled several experiments on venturi-tube flowmeters smaller than those permitted by the ISO specification [43]. Several of these studies suggest venturi-tubes perform consistently at smaller sizes and lower Reynolds number, but the user must experimentally determine the discharge coefficient over the operating range.

A drawing of the venturi is shown in Figure 5 with dimensions shown in millimeters and degrees. The throat diameter was selected to produce a pressure differential of approximately 70 kPa (10 psi) at 20 liters/minute of Solar Salt to maximize the range of the pressure transducer diaphragms in contact with the salt. The convergent, throat, and divergent sections of the venturi were formed using electrical-discharge machining (EDM) from a 38 mm (1.5 inch) 316/L stainless steel bar stock. EDM was used to achieve the tight tolerances and sharp corners recommended by the ISO specification. The 1.02-mm pressure tap into the venturi throat was also formed by plunge EDM to prevent undesirable edges/burrs within the throat. The tolerance reported by the manufacturer is +/- 0.05 mm. The entrance tube bore was machined 5 diameters upstream to match the diameter of the venturi convergent to within 0.03 mm to minimize flow disruptions at the entrance. Finally, the mating ends of both the entrance and exit tubes were turned down to fit snuggly in the counterbore on either end of the venturi body prior to welding.

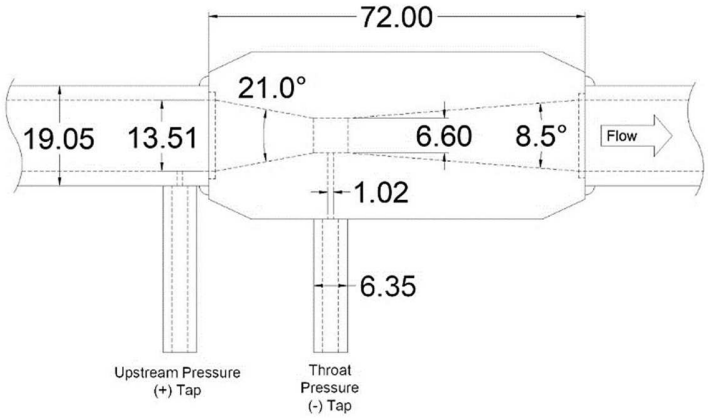

Figure 5. Dimensions of custom venturi flowmeter (shown in millimeters)

A pin-gauge was used to confirm the entrance and throat diameter of 13.51 ± 0.05 mm and 6.60 ± 0.03 mm, respectively. Due to the discrepancies between this small venturi and the ISO requirements, the venturi's performance was first examined with room-temperature water versus a Coriolis flow meter (Foxboro CFS10) and later in nitrate salt versus a vortex shedding flow meter (Foxboro 83F-A01). The results of this calibration are used to experimentally determine the discharge coefficient and bound the error associated with this flow meter for propagation of error into the thermal hydraulic results. Equation 3 is derived from Bernoulli's principle for an incompressible medium passing through a restriction. The discharge coefficient C_D, accounts for the non-ideal conversion of static pressure to an increase in flow velocity as the fluid passes through the venturi convergent, thus typically taking on a value less than unity. The discharge coefficient can be determined experimentally during flow calibration using the measured volumetric flow rate ($\dot{V}$) and pressure drop (ΔP). The throat area (A_t) is 34.25 mm^2 and throat-to-pipe diameter ratio (β < 1) is 0.4887. Thermal expansion of the venturi throat was incorporated into the calculation of discharge coefficient during salt testing. However, the expansion effect was less than 10% of the propagated error for any given measurement. Finally, the fluid density (ρ) was determined using the average of fluid temperatures on either side of the venturi and the thermophysical property polynomials for water and Solar Salt.

$$\dot{V} = C_D \frac{A_t}{(1-\beta^4)} \sqrt{\frac{2\,\Delta P}{\rho}} \quad [3]$$

Over 400 data points were collected between the two fluids. Water testing was conducted before and after installation to the salt test section, while isothermal salt data was collected during salt friction factor tests. Additional data collected during heat transfer testing is plotted, although the vortex and venturi flowmeter were at different temperatures due to their placement on either side of the heat exchanger as shown in Figure 4. Since a vortex flow meter measures flow rate based on the generation of vortices within the flow, it is limited to flow rates of ~ 6 L/min to maintain the Reynolds number within the sensor is greater than 10,000. Furthermore, the vortex shedder has a maximum operating temperature of 425°C which prevented its use during all testing. Figure 6 shows the calculated discharge coefficient versus the Reynolds number at the venturi inlet for the water and nitrate salt datasets. The venturi Reynolds number is calculated using the entrance pipe diameter (13.51 mm) and the volumetric flow rate measured by the calibrating flow meter. As mentioned above, a Foxboro Coriolis was used during water testing and the Foxboro vortex shedder was used during in-situ salt testing. The salt's density and viscosity were calculated using incompressible properties proposed by [44] at the average of the venturi inlet/outlet temperatures. Meanwhile, the average of the inlet/outlet temperatures and absolute pressure indicated by a bourdon-gauge were used to evaluate the properties of water [45]. At low flows, the discharge coefficient determined by equation 3 with salt is observed to slightly exceed unity. This behavior has been observed during testing of two similar venturi tubes tested with nitrate salt within the Thermal Hydraulics Laboratory at UWM. Similar behavior has been summarized by [43] as well. The cause of this behavior, typically observed below and around Reynolds of 10,000 needs further investigation. While acceptable performance was achieved in this venturi, most laboratory and pilot-scale venturi flow meters operate below the ISO lower-limit, emphasizing the need for further research on high-temperature salt venturi flowmeters.

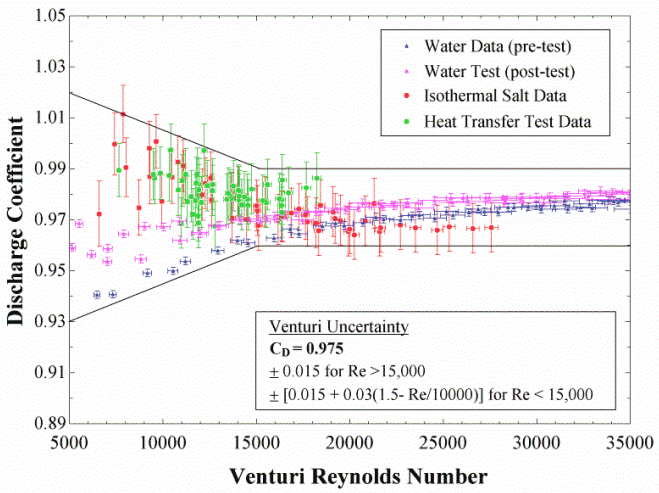

Figure 6. Venturi discharge coefficient versus Reynolds number with water and nitrate salt

Since the salt and water datasets converge around Re = 15000, a constant discharge coefficient of 0.975 +/- 0.015 is assigned to the venturi when the entrance Reynolds number exceeds this value. Below a Reynolds number of 15000, a linearly increasing error component is added to the nominal +/- 0.015 to encompass both the salt and water data in this range. The error associated with the venturi discharge coefficient, bounded by solid black line in Figure 6, was typically the dominant error associated with friction factor and heat duty determination on the salt side. After this thorough investigation of the venturi's performance, the authors were confident that the salt flow rate was known within 1.5 – 2.5% under most operating conditions.

3.6. Uncertainty Propagation

The uncertainty associated with the thermal hydraulics measurements below originate from either propagation of instrument uncertainty or the variance of these measurements over the period of acquisition. This section addresses how the combined uncertainty and variance in the measured hydraulic and thermal performance parameters, propagate into the dimensionless results. Tables 4 and 5 shows the manufacturer's uncertainty for each instrument used in the calculation of Reynolds number, Fanning friction factor, or overall conductance for the CO_2 and salt streams, respectively.

Due to the limitations of CO_2 flow instrumentation in earlier test campaigns, two flow meters were used under high-flow conditions. The error of these was added together to determine the CO_2 flow rate uncertainty for these tests. For most of the friction factor data and all heat transfer data a single, larger flow meter was used. Two differential pressure transducers measured pressure loss across the entire DBHE and the core region separately. The error associated with these varies with respect to the range/span setting employed for the given test. In the calculation of friction factor, differential pressure error dominates at low flow rates, while temperature error dominates in Reynolds number uncertainty at high flow rates, due to viscosity temperature-dependence. During heat transfer testing, the temperature uncertainty was typically the greatest contributor to propagated error of the overall conductance.

Table 4
CO_2 – Side Instrument Type and Uncertainties

Instrument	Uncertainty
Mass Flow Rate	
Siemens MASS2100/ EH CubeMASS DCI	± 0.3% of measured value
MicroMotion F050P	± 0.15% of measured value
Absolute Pressure	
Rosemount 3051S	± 0.15% of measured value
Differential Pressure*	
Siemens Sitrans DSIII	± 0.3 – 0.5% of measured value
Yokogawa EJA110E	± 0.04 psi
Fluid Temperatures	
K-type Thermocouple	± 1.1 K or 0.4% of reading

* Depends on span settings which were varied to minimize error

On the nitrate salt side of the heat exchanger, the venturi flowmeter uncertainty was determined experimentally as described in Section 3.5. The error in discharge coefficient with respect to Reynolds number and error of the differential pressure transducer connected to the venturi were both propagated into the flow rate calculation. The vortex shedding flow meter which provided a secondary flow measurement is also provided, as this uncertainty affected the determination of the venturi's performance. Although the vortex flowmeter has better accuracy compared to the propagated uncertainty of the venturi, all thermal hydraulic results employ the flow measurement from the latter for consistency between datasets. Differential pressure across the venturi and across the salt-side of the DBHE were measured by separate pairs of remote diaphragms which were maintained at 270 ± 15°C during all tests. The salt-side flow was stopped frequently to record the zero-flow indication (ZFI) from both transmitters. Whenever the change in ZFI exceeded the manufacturer's uncertainty (± 0.03 psi), the observed change was used for error propagation. Typically, the change in ZFI was between ± (0.002 – 0.02) psi when the diaphragms were bled to remove any trapped air. The two pressure transducers employed during water testing of the venturi and salt-side of the DBHE are also included in Table 5. In the calculation of friction factor, differential pressure error across the heat exchanger dominated at low flow rates, while the venturi discharge coefficient uncertainty dominated at high flow rates. During heat transfer testing, both temperature and flow rate uncertainty played a significant role. Operating a moderate salt flow rates (8 – 15 L/min) with large temperature differentials (> 75°C) provided the best heat transfer data.

Table 5
Salt – Side Instrument Type and Uncertainties

Instrument	Uncertainty
Volumetric Flow Rate	
Venturi Flow Meter	± 1.5 – 3 % (evaluated for each data point)
Foxboro 83F Vortex	± 0.5 – 2%
Differential Pressure	
Rosemount 3051 w/ 1199 diaphragms	± 0.03 psi or Δ zero flow indication (ZFI) reading
Siemens Sitrans DS III	*± 0.35% of measured value*
Yokogawa EJA110E	*± 0.04 psi*
Fluid Temperatures	
K-type Thermocouple	± 1.1 K or 0.4% of reading

*Instruments in italics used for water testing

4. Thermal & hydraulic performance results

Several studies have been conducted on DBHE with zig-zag geometries, although its geometric complexity has resulted in significant variation in the calculation of dimensionless parameters. Differences in plate stacking arrangement, uncertainty in the channel dimensions, and inconsistent definitions of the hydraulic diameters and flow or heat transfer areas have slightly clouded the literature. For all results presented below, the flow is assumed to be uniformly distributed among the microchannels and thermophysical properties are evaluated at the average fluid temperature for each stream. The Fanning friction factor and Nusselt numbers are calculated based on experimental results using the geometric definitions provided in Table 2. The 316/L component examined here utilizes a CO_2 side geometry nearly identical to a DBHE examined by Katz [10], who was also involved with the same IRP addressing technical development of compact heat exchangers. The analysis method described below was developed in collaboration with this author to present comparable results.

4.1. Fanning friction factor determination

Pressure drop tests were performed under isothermal conditions to calculate the Fanning friction factor of the core region for each fluid. CO_2 (cold-side) tests were conducted first, with the NSL in a shutdown state. The salt-side was open to the atmosphere while the CO_2 temperature remained 12 +/- 2°C for all pressure drop tests. Later, isothermal tests on the salt-side were performed without CO_2 pressure on the other side of the exchanger. Additional salt-side tests were conducted between heat transfer tests by stopping the CO_2 flow and allowing the exchanger to approach isothermal conditions. Natural CO_2 circulation was not possible due to the WisCO_2 pump valves remaining closed during salt friction factor tests; thus, the salt-side results were not affected by the presence of CO_2 on the cold-side. Several water pressure-drop tests were also conducted on both sides of the heat exchanger to compare the water-derived friction factor with the CO_2 and nitrate salt results.

Differential pressure transducers connected to the pressure taps protruding from the core, as shown in Figure 1, measure the core losses over a known length of zig-zag channel (L_{zz}) for each fluid. During CO_2 and water tests, an additional differential pressure transducer simultaneously measured the overall pressure loss at the terminal temperature measurement ports on the inlet/outlet nozzles. During the final salt test, the oil-filled salt pressure transducers were relocated to auxiliary pressure ports near the inlet/outlet nozzles to quantify the overall salt-side pressure losses. These measurements are compared to the core loss predicted by the friction factor correlation to determine the proportion of total pressure loss due to the header regions. Equation 4 is used to calculate the expected pressure drop in a compact heat exchanger [46]. The four terms represent the loss contribution by the inlet contraction to the microchannels, flow acceleration due to density change, expansion upon exiting the microchannel region, and frictional losses (ΔP_f) in the microchannels. While using the core pressure taps to compute friction losses, the terms for entrance and exit effects can be eliminated. Furthermore, during isothermal conditions, the fluid acceleration effect is negligible ($< 0.03\%$) for both fluids. All data points used have acceleration terms well within the measurement uncertainty of the respective pressure transducer. Therefore, the Fanning friction factor is calculated for the zig-zag geometry using the simplified equation 5.

$$\Delta P = \frac{G^2}{2\rho_{in}}\left[(1 - \sigma^2 + K_c) + 2\left(\frac{\rho_{in}}{\rho_{out}} - 1\right) + (\sigma^2 - K_e - 1)\left(\frac{\rho_{in}}{\rho_{out}}\right)\right] + \Delta P_f \quad \textbf{[4]}$$

$$\Delta P_f = f_F \left(2\frac{G^2}{\rho}\frac{L_{zz}}{D_h}\right) \quad \textbf{[5]}$$

Using the core flow areas shown in Table 2, the core mass flux (G) is calculated for each data point. Mass flux on the CO_2 side varies from 185-2600 kg/m^{2}s while on the salt side it varies from 90-950 kg/m^{2}s. The fluid density (ρ) is calculated using the average fluid temperatures, the Span-Wagner equation of state [47] and the polynomial approximation reported by Pacheco [44], for CO_2 and Solar Salt respectively. The length of the core region (L_{zz}) reflects the effective flow length or path length of the zig-zag channel between the pressure taps. Some researchers have elected to use the shortest linear/axial distance between taps to calculate friction factor. This is thought to be incompatible with the (semi-) elliptical representation of the channel cross-section which remains nearly constant along the entire core. Neglecting to account for the additional length resulting from the tortuous flow path results in a higher calculated friction factor, which may skew interpretations of hydraulic and thermal performance trade-offs with respect to zig-zag angle. Conversion of these results to a straight channel assumption can be achieved by dividing the calculated Fanning friction factor by the cosine of the bend angle (θ) with respect to horizontal.

The calculated friction factor (f_F) on the salt-side is plotted versus Reynolds number in an individual microchannel in Figure 7(a). Due to the relatively high density and dynamic viscosity of the nitrate salt, flows of up to 18 L/min divided

among the 224 elliptical flow passages remain well within the laminar regime. Since the corrugated flow path is constantly disrupting flow development, the friction factor is 3 to 5 times greater than the analytical solution for laminar flow through a straight, circular duct. Due to a ~50% reduction in the salt's viscosity when increasing from 350° to 550°C, the range of Reynolds numbers is significantly extended at higher temperatures. Furthermore, water data which has similar kinematic viscosity to the salt at 550°C yields friction factor results which show excellent agreement with the salt data over the entire range.

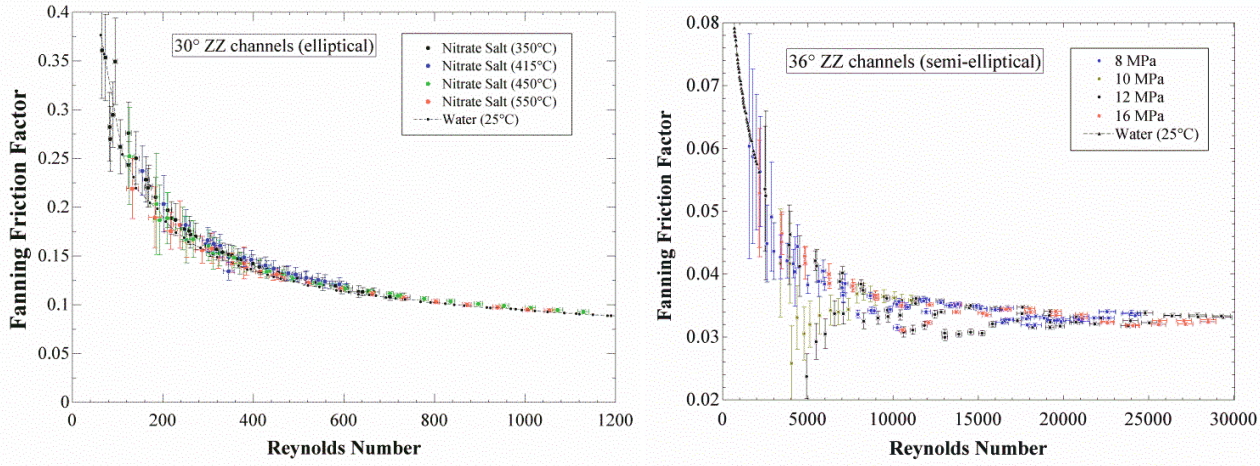

Figure 7. Fanning Friction Factor measured across the core: (a) salt – side, (b) CO_2 – side

The plot in Figure 7(b) shows the friction factor measured with supercritical CO_2 versus Reynolds number in the 240 semi-elliptical channels. Due to the very low dynamic viscosity of sCO_2 the isothermal results extend well into the turbulent regime despite its high density (~ 900 kg/m^3) and operate in a similar mass flux range as salt and water. A significant amount of scatter in the data is observed near the transition region. While most data points do conform to a power-law dependence upon Reynolds number, uncertainty is high below a Reynolds number of ~8000. The large error bars in this range are due to the low magnitude of the pressure loss signal. The relative error in pressure drop becomes quite large, which propagates into a large uncertainty in friction factor. Each salt and CO_2 data point in Figure 7 represents a minimum of 1-minute data acquisition at 2 Hz (120 data points). The raw data collected during each 1-minute test was averaged prior to non-dimensionalization. Any data point with pressure-drop or flow variation greater than the associated instrument's uncertainty was removed from the regression dataset.

Water data was also collected on the CO_2 – side after removal from the WisCO_2 loop. This data extends the range of friction factor data deep into the laminar regime. Due to the drastic difference in properties, namely viscosity, the pressure drop magnitude is large and thus its uncertainty is minimal for this dataset. While the water and CO_2 data do conform to a clean trend, it is difficult to compare their agreement since the maximum and minimum flow capabilities of the water and CO_2 loop only overlap over a very limited range of Reynolds number. Although the water data from the CO_2 side does not provide validation of the CO_2 friction factor data, is does provide useful quantitative data to a designer or potential component user considering the use of semi-circular channels for high-temperature liquid coolants such as salt or liquid metals.

Figure 8 shows the raw pressure drop results from several water loss tests to further this comparison between the semi-elliptical and elliptical channels. Figure 8(a) shows results from water tests on the salt side. This includes two sets of data between salt tests, and two sets after removal from the test facility. While seeking to answer questions regarding draining or plugging problems in the early phases of salt testing, the salt lines were cut using a wheeled pipe cutter to prevent sending metal burrs or abrasive cutting materials into the piping. A few data points revealed slightly elevated overall pressure drop (~10% increase), but due to the high solubility of Solar Salt in water any residual salt quickly dissolved. Initial measurements of pressure drop suggested a general lack of channel plugging in the heat exchanger due to incomplete salt drainage. This result was complemented by non-destructive examination performed immediately after the final salt test. Furthermore, flow testing was performed in both directions to examine the symmetry of heat exchanger with respect to flow direction. Upward and downward flow datasets are provided for both sides of the heat exchanger. No statistically significant difference between the datasets could be determined, therefore data for both flow directions were used in the friction factor regression discussed below.

Figure 8(b) presents pressure drop data from the water test performed on the CO_2 side of the heat exchanger after it was removed from WisCO_2 – NSL test facility. The core losses exhibit a higher core pressure drop compared to the salt-side at the same mass flux through the core region. This is not surprising given the more aggressive bend angle, shorter pitch between bends, and smaller hydraulic diameter. Meanwhile, the overall losses are lower than the on salt-side which is primarily an artifact of the compact and relatively simple header/transition geometry employed on the high-pressure CO_2

side. The salt-side header region has a somewhat convoluted flow path with several bends to avoid the CO_2 pressure boundary, which results in a higher proportion of pressure losses resulting from this region. More discussion on header/transition losses in provided in the next section.

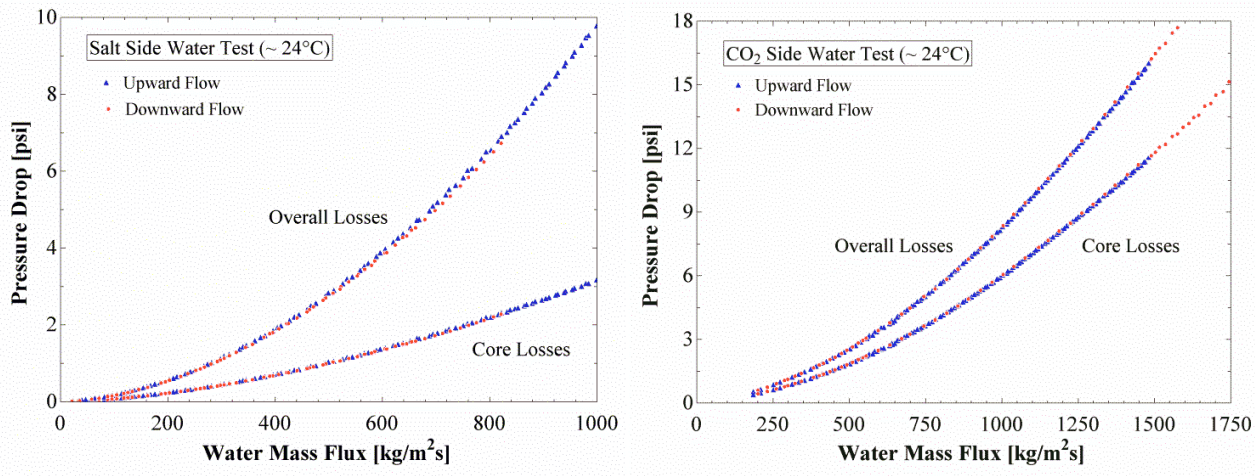

Figure 8. Pressure losses across the heat exchanger during water test: (a) salt – side, (b) CO_2 – side

A friction factor correlation was developed for each fluid-geometry pair, to provide a concise representation of the isothermal pressure drop datasets collected with sCO_2, Solar Salt, and water. The pressure drop data was processed in Engineering Equation Solver (EES) to make use of its built-in thermophysical property calculation and numerical error propagation capabilities. The calculated Fanning friction factor and Reynolds number were then exported to MATLAB for non-linear regression using the 'nlinfit' functionality.

Table 6 presents correlations for each fluid-geometry pair. A functional form including two or three coefficients was selected to minimize the residual sum of squares, also known as the sum of the squared residuals. The Reynolds range associated with each dataset is provided and should be regarded as firm boundaries on the use of these correlations. Recall that attempts to compare these correlations with those in previous literature requires careful attention to the definition of geometric parameters, especially the hydraulic diameter and flow length. The accuracy of these correlations is examined in Section 5.1 by making use of non-isothermal pressure drop data collected during several days of heat transfer testing.

Table 6
Fanning friction factor correlations from experimental data

Geometry	Correlation	Reynolds Range	Dataset Size (N)/ Residual Sum of Squares (RSS)
CO_2 – side (37° semi-elliptical)	$f = 1.022\,Re^{-0.537} + 0.028$	Re = [500, 30000]	N = 249: RSS = 6e-3
CO_2 – side (water test)	$f = 0.774\,Re^{-0.425}$	Re = [200, 1950]	N = 184: RSS = 4e-4
Salt – side (30° elliptical)	$f = 5.419\,Re^{-0.664} + 0.042$	Re = [60, 1100]	N = 138: RSS = 4e-2
Salt – side (water test)	$f = 4.477\,Re^{-0.639} + 0.041$	Re = [100, 1650]	N = 395: RSS = 2e-3

4.2. Header Losses

The headers of the heat exchanger are defined as the region between the pipe nozzles welded to the diffusion-bonded core and the region of the core whose cross-section consists entirely of zig-zag microchannels. The heat exchanger examined here employs internal headers which means fluid distribution to the individual microchannels occurs within the diffusion-bonded core. Alternatively, external headers are forged shells or sectioned pipes which are welded to the core after diffusion-bonding of the microchannel core. Several comparisons between internal and external headers have been provided along with proposed design rules for the attachment of external headers and structural attachments in [7]. In summary, internal headers can reduce the post-bond welding requirement and are likely to maximize heat exchanger conductance (UA) per unit mass. Depending on inspection requirements of traditional full-penetration welds versus diffusion-bonds, further cost reductions could be realized during component operation in a nuclear plant by reducing the volume of weld that must undergo non-

destructive, in-service inspection. VPE has produced many high-pressure cores with their internal header designs which reduce weight, cost, and fabrication time. A recent study with a 316/L stainless-steel hydrogen precooler revealed excellent fatigue strength at room-temperature [48]. This study emphasizes why diffusion-bonded components are a great option for applications demanding the highest level of integrity and reliability.

Given the technoeconomic advantages of internal headers/flow distributors, their layout and geometry are typically not disclosed by vendors. Although they were revealed by x-ray examination, no geometric details of the internal headers are provided here. Pressure loss measurements collected across these regions are still provided since they have not been examined by previous studies. Generally, header losses are assumed to be negligible due to the inability to measure these losses during testing. The pressure drop across the header region is presented as a ratio of the overall pressure loss for each side. Non-dimensionalization of these results was not performed since this would require specification of several header dimensions shown in equation 4. The results shown here serve to provide a benchmark of header losses in a commercially available component of known overall volume and core flow area. The inlet and outlet headers are mirror images of one another, and their design is expected to remain similar for heat exchangers with wider plates to include more flow passages. Furthermore, a longer heat exchanger will have headers regions of roughly fixed size, which would reduce the header loss ratio (P^*) defined by equation 6.

$$P^* = \frac{\Delta P_{total} - \Delta P_{core}}{\Delta P_{total}} \quad \textbf{[6]}$$

On the CO_2 – side, P^* is easily determined by using pressure loss measurements across the nozzles and the core region, which were collected simultaneously by separate differential pressure transducers. The header loss ratio is plotted versus the mass flux within the zig-zag core region in Figure 9. The data shows little dependence on Reynolds number or CO_2 pressure for these isothermal tests conducted at 12 +/- 2°C. The large variance within a data set may be due to non-uniform flow distribution and turbulent effects that could not be explored further. The water data, by comparison shows a nearly constant header loss ratio. One can conclude however, that approximately half of the overall pressure loss across the heat exchanger occurs in the entrance and exit transitions between the nozzle and core region. Several previous studies attempt to neglect header losses to calculate core friction factor which is likely to result in core friction factors much higher than those provided above. While internal headers may provide a significant economic incentive, external headers should be used in future thermal hydraulic studies seeking to focus on the microchannel behavior by minimizing the header effect.

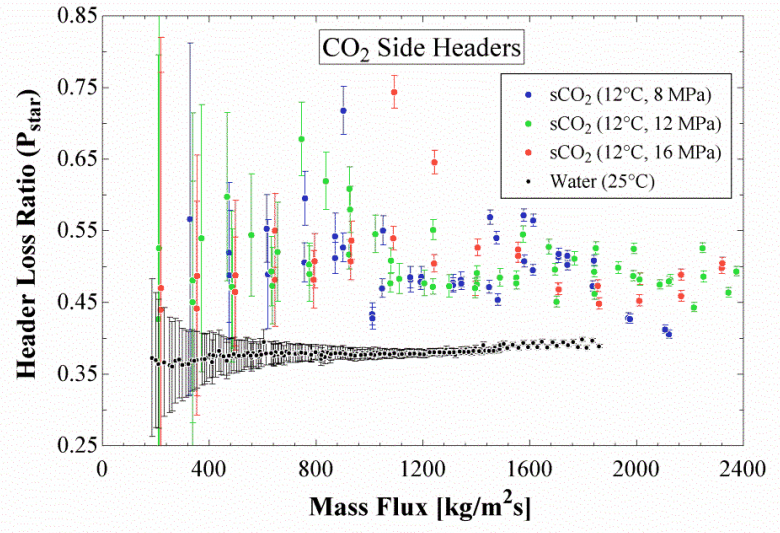

Figure 9. CO_2 header pressure loss ratio versus mass flux

Meanwhile on the salt-side, the remote pressure-sensing diaphragms had to be relocated to a different set of pressure taps between test campaigns to quantify the overall pressure drop. The flanged diaphragms and their heated sleeves require more space than the CO_2 sensing lines and therefore could not be located as closely to the heat exchanger. During the final test campaign, the diaphragms were moved to pressure measurement ports intersecting the entrance/exit salt piping. The correlation generated from the isothermal friction factor tests in Table 6 was used to estimate core losses for each flow condition. In the same manner as the CO_2 side, the header loss pressure ratio is estimated using data at salt temperatures between 325 – 415°C. This range was selected to take advantage of the salt's significant viscosity change between these temperatures. The upper temperature limit was imposed by the vortex flow meter used to validate the performance of the

venturi flow meter, as described above. The header loss ratio is plotted versus mass flux in the microchannel core in Figure 10. After removal of the heat exchanger from the salt loop, core and overall pressure loss measurements were collected simultaneously with water. Overall pressure drop was measured at the same measurement ports as the salt transducers. During the creation of Figure 8(a), the overall core loss was measured on the thermocouple ports which are located closer to the heat exchanger core. The additional 30 cm of salt piping between the thermocouple ports and the auxiliary salt pressure measurement ports accounted for a 4 - 6% increase, therefore the header loss ratio presented below can be considered as a conservative estimate.

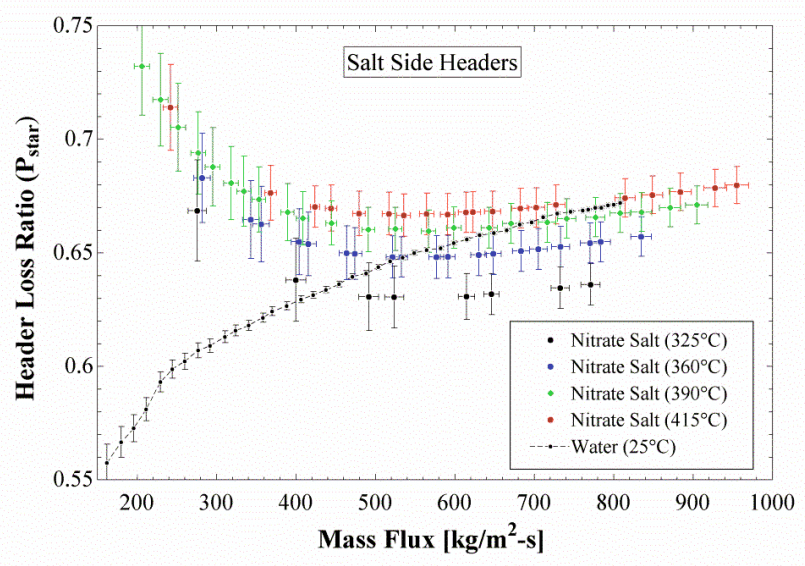

Figure 10. Salt-side header pressure loss ratio versus mass flux

Figure 10 shows two notable trends. First, the header losses are relatively constant versus salt flow rate or mass flux. When salt viscosity is lower (at higher temperatures), header losses increase slightly. When plotted versus Reynolds number the salt datasets converge at high flow rates. Secondly, while water provides similar results to salt at moderate mass flux, they diverge at lower flow rates. Fortunately, for heat exchanger designers seeking to use water as a surrogate test fluid, this divergence occurs well below the design point, at Reynolds < 500. In summary, the salt-side header losses constitute ~ 65% of the total pressure loss. This shows a clear need for further development of compact heat exchanger headers utilizing liquid coolants. External headers may provide a useful option, although these were not feasible with the CO_2 header configuration employed in this component. Inspection and cleaning requirements in liquid geometries may also require the use of external headers to gain more direct access to the individual microchannels. Given the requirement for a low-cost component, where internal headers were selected for lead time considerations, these results should not be interpreted as ideal performance. Future researchers should focus closely on the liquid-side header design to minimize header losses, and potentially propose their own geometry for a more detailed hydraulic investigation of the header/transition region.

4.3. Heat transfer testing

Once isothermal friction factor tests were performed on the both the sCO_2 and nitrate salt sides of the heat exchanger, both flow loops were operated simultaneously to measure the heat transfer performance of the component. Figure 11 shows the heat duty of the nitrate salt stream versus the CO_2 stream at each of the experimental data points. The error bars represent the measurement uncertainty associated with the flow rate and terminal fluid temperatures of each stream. Since the thermophysical properties of the salt are presented in incompressible form [44], absolute pressure uncertainty was also considered for the CO_2 stream. Nearly all data points above 3 kW of heat transfer show heat rate parity within ± 10%. The trend shows greater heat removal from the salt stream, compared to heat input to the CO_2 stream, indicating some heat losses from the component. A separate test was performed to bound heat losses from the heat exchanger. This test, discussed in Section 4.5, conservatively bounded the heat losses to less than 200 W. For data points at low heat duty (< 5 kW) factors such as large venturi flow meter uncertainty and low temperature differential result in some points lying outside the ± 10% boundary shown in Figure 12. Since the observed heat losses lie within the propagated uncertainty of heat transfer rate for

each fluid, these losses are assumed to be acceptable, and no correction is made to the calculation of observed heat transfer or overall conductance. Furthermore, any data point exhibiting a difference in stream heat duty greater than 8%, or average heat duty less than 3 kW was omitted from the analysis presented below.

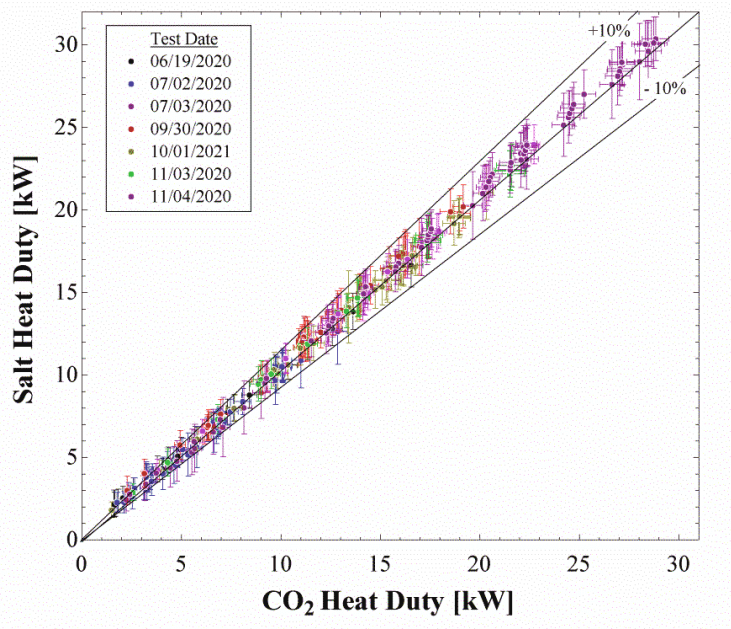

Figure 11. Parity plot of heat rate of hot and cold fluids

Several factors limited the range of conditions under which the heat exchanger could be examined. On the salt side, the salt inlet temperature was varied from 350°C to 550°C. The lower limit allowed for temperature drops across the heat exchanger of up to 75°C, without risking crystallization/freezing in the venturi flowmeter and return piping. The upper temperature limit was ~550°C, since operating at steady-state conditions above this temperature resulted in the loop's heater elements being above 700°C. Solar Salt decomposition is known to be significant above 600°C, so the duration of operation at this temperature was limited to a few hours [49].

On the CO_2 side, the inlet pressure to the heat exchanger varied between 10-16 MPa. While the heat exchanger and other supporting equipment in the WisCO_2 loop can operate up to 22 MPa, the flow and pressure instrumentation used in this work was limited to 16 MPa (2320 psi). The CO_2 inlet temperature is governed by the performance of the CO_2 recuperator, which is significantly larger than the salt – CO_2 heat exchanger. Initial tests did not bypass any flow around the cold-side of the recuperator. Thus, the CO_2 mass flow rate is the same on both sides of the recuperator. Due to the high heat transfer area and therefore conductance of the recuperator, the CO_2 inlet temperature remained approximately 50-70°C below the salt inlet temperature regardless of flow rate. The CO_2 inlet temperature to the salt heat exchanger was later reduced by bypassing some of the cold stream around the recuperator before recombining near the recuperator outlet, as shown in Figure 4. Reducing the CO_2 inlet temperature was the best method to increase the heat rate across the exchanger once a full set of flow sweeps had been conducted without recuperator bypass.

Several of the heat transfer test conditions have been plotted in Figure 12, which shows CO_2 versus Solar Salt mass flow rate. Lines of constant capacitance ratio (C_R) have been overlaid on the plots to reflect the similarity in mass-specific heat capacity of these two fluids at 400°C. The CO_2 capacitance is calculated at 16 MPa to match the most common operating pressure. Salt flow rate was constrained by the wire mesh filters employed in the test section during the initial tests. A maximum of 0.44 kg/s could be achieved during the final heat transfer test campaign as the filtering technique improved. The minimum flow rate was approximately 0.08 kg/s due to the low accuracy of the venturi below this flow rate. Meanwhile, the CO_2 flow rate was limited to 0.325 kg/s due to the maximum pump speed. Other limitations are combined effects of both flow loops. At high CO_2 and salt flow rates, heat input became a limitation. In the final test campaign, nearly 30 kW was transferred across the heat exchanger which required near maximum power input from the salt heaters and maximum heat rejection by the WisCO_2 loop chiller and the facility's chilled water system. Furthermore, while running at high CO_2 flow rates with moderate salt flow rate to approach a balanced condition (C_R = 1), the heater temperatures in the salt loop would exceed 700°C due to low flow velocity past these heater elements. To minimize decomposition of the salt, operation under these conditions was reserved for last and limited in duration.

The final constraint on the test envelope was imposed by the analysis method. Referring to the lines of constant capacitance ratio (C_R) in Figure 12, one can observe that nitrate salt stream usually had the maximum heat capacitance rate. If the capacitance ratio drops below ~0.4, the CO_2 outlet temperature approaches the salt inlet temperature, or vise-versa. When the fluid temperature difference on either end of the heat exchanger approaches the thermocouple uncertainty (±1.3 – 2.3°C), the propagated error associated with the overall conductance (UA) becomes exorbitantly large. Therefore, the lines of constant capacitance ratio provide a rhombus-shaped operating envelope for the coupled WisCO$_2$ – NSL test facility.

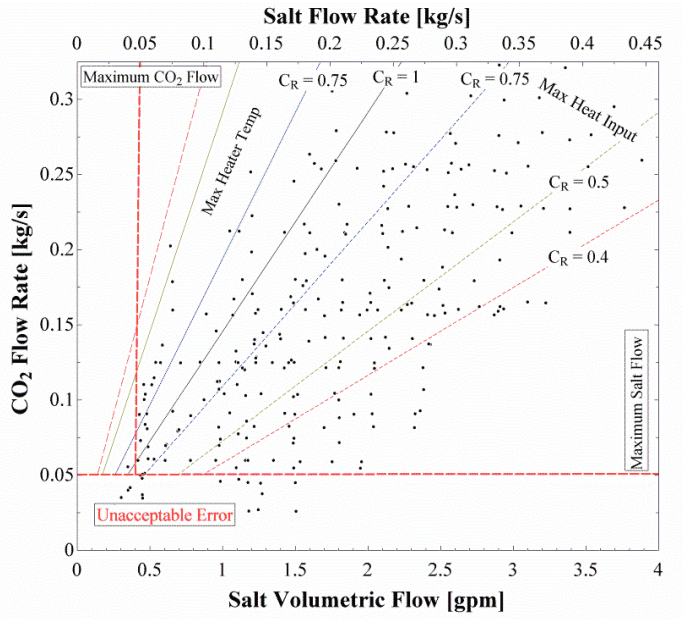

Figure 12. Operating Envelope of the WisCO$_2$ – NSL test facility

Due to the large thermal inertia of the NSL and the transient effects due to flow changes, significant experiment run time was spent waiting for thermal equilibrium. Therefore, a quantitative definition is provided for the term "steady-state" used in this paper. After adjusting either mass flow rate, the operator would also adjust the salt heater power and wait several minutes for the terminal temperatures to approach stable values. Steady-state was defined as a change of less than 0.4° C per minute, as this could be achieved in ~10 minutes after the perturbation. Once stable, flow, temperature, and pressure drop data were collected for at least 5 minutes at a rate of 2 Hz to capture good statistics for each measurement. This definition was informed primarily by the 0.4% error associated with the K-type thermocouples used for terminal temperature measurement. At 500°C, this suggests at error of ± 2°C which aligns with the maximum nominal temperature drift of 2°C during a 5-minute data acquisition at this definition of "steady-state".

4.4. Dimensionless heat transfer coefficient

The heat transfer rate between the nitrate salt and sCO$_2$ streams was used to determine the overall conductance of the heat exchanger. The overall conductance (UA) was calculated using the log-mean temperature difference method and the average heat duty of each data point as shown in equation 7. Like previous DBHE studies, the compact nature of these geometries prevents direct measurement of wall temperatures or fluid measurements along the length of the component. Due to this limitation, the heat transfer coefficients for each stream are deduced from a heat transfer network including the two fluid convection resistances and a conduction resistance for the separating wall, as shown in equation 8. The heat exchanger was not discretized along its length due to lack of detailed knowledge of the temperature distribution along the longitudinal axis of the component. To overcome this limitation, the heat exchanger was examined under the full range of the test facility's capabilities to examine how the two unknown convection coefficients ($\bar{h}_H$, $\bar{h}_C$) affect the measured overall conductance.

$$UA = \frac{(Q_C+Q_H)}{2*LMTD} = Q_{AVG} * \ln\left(\frac{T_{H,out}-T_{C,in}}{T_{H,in}-T_{C,out}}\right) * [T_{H,out} - T_{C,in} - T_{H,in} + T_{C,out}] \quad [7]$$

$$\frac{1}{UA} = \frac{1}{A_{s,H}\,\bar{h}_H} + \frac{\delta}{A_w\,k_w} + \frac{1}{A_{s,C}\,\bar{h}_C} \quad \textbf{[8]}$$

Since the microchannel geometry is different for each fluid, heat transfer areas from Table 2 of 0.405 and 0.332 m^2 were used for the salt ($A_{s,H}$) and CO_2 sides ($A_{s,C}$), respectively. The conduction distance (δ) was determined by examining a unit cell of each microchannel. The (semi-) elliptical channel flow area is subtracted from the product of the unit cell width (2.74 – 3.05 mm) and shim height (1.47 mm). This 'cross-sectional wall area' is divided by the unit cell width to obtain a smeared conduction thickness across the unit cell. Since this thickness is 0.96 and 1.08 mm on the CO_2 and salt-side respectively, the conduction distance (δ) is approximated to be 1 mm. This aligned with the assumption made by Katz [10]. The thermal conductivity of the 316/L wall is evaluated at the average of all four terminal temperatures using conductivity data published in [50]. The conduction wall area per plate is defined as the product of the width of salt-side unit cell (2.74 mm), the number of flow passages (16 per plate), and the heat transfer length ($L_{HT} = 270mm$) from Table 2. Recall there are 14 salt layers alternatively stacked with 15 CO_2 layers. Since the outermost CO_2 layers only see heat flux from one side, the total conduction wall area (0.166 m^2) is determined by multiplying the per-plate conduction area by 14 to represent the number of interfaces between the salt and CO_2 layers.

To express the convective heat transfer behavior in dimensionless form, the heat transfer coefficient is replaced by its representation in Nusselt form. A power law relationship of the form shown in equation 9 is assumed for both fluid streams. The one-third power dependence upon Prandtl number is fixed due to lack in significant variance of the CO_2 Prandtl number during testing. A more controlled heat transfer study, with wall temperature measurement would be better suited to examine the Prandtl-dependence of molten salts in compact geometries. Considering the novel use of molten salt in a zig-zag geometry, Prandtl dependence was fixed to constrain the non-linear regression for correlation development. Fixing the Prandtl dependence also facilitates straight-forward conversion to the Colburn j-factor shown in equation 10. By substituting the assumed Nusselt power law relationship into the heat transfer resistance network, equation 11 represents the nonlinear regression model which was fit to the experimental data.

$$\overline{\boldsymbol{Nu}} = \frac{\bar{h}D}{k_f} = a \cdot Re^b \cdot Pr^{\,1/3} = \boldsymbol{j} \cdot Re \cdot Pr^{\,1/3} \quad \textbf{[9]}$$

$$\boldsymbol{j} = a \cdot Re^{(b-1)} \quad \textbf{[10]}$$

$$\frac{1}{UA} = \frac{D_H}{A_{s,H}\,k_H\,a_1\,{Re_H}^{b_1} Pr_H^{\frac{1}{3}}} + \frac{\delta}{A_w\,k_w} + \frac{D_C}{A_{s,C}\,k_C\,a_2\,{Re_C}^{b_2} Pr_C^{\frac{1}{3}}} \quad \textbf{[11]}$$

The channel dimensions in Table 2 are used to compute the relevant dimensionless numbers for each fluid. The Reynolds and Prandtl numbers are evaluated using the average of the inlet and outlet fluid temperatures for each stream. The inlet pressure is used for sCO_2 property determination, while the Solar Salt properties are provided in incompressible form and therefore do not require an inlet pressure. Only differential salt pressure was measured across the heat exchanger and venturi flowmeter.

As the temperature changes throughout the component, the Reynolds number will also change. At higher CO_2 pressures, viscosity and density have less dependence on temperature which results in a less significant change in Reynolds number. Except for viscosity, all salt properties exhibit gradual, near-linear trends versus temperature. Viscosity variation was utilized during friction factor testing to extend the Reynolds number. To minimize the effect of the viscosity non-linearity on the heat transfer behavior, salt temperatures were typically kept above 350°C during heat transfer testing. Using 238 experimental data points spanning various CO_2 pressures/temperatures and salt inlet temperatures, the overall conductance, average Reynolds (Re_H, Re_C) and Prandtl (Pr_H, Pr_C) numbers for each stream were calculated using the measured mass flow rates and terminal temperatures.

The variables were then fit in MATLAB to determine the unknown coefficients $\{a_1, b_1, a_2, b_2\}$ which minimize the cumulative error in prediction conductance (UA). The fitted Nusselt correlations are shown in Table 7 along with the Reynolds and Prandtl ranges from the experimental data. By operating at conditions far from the critical point, the sCO_2 properties do not vary significantly with temperature or pressure, and therefore the Prandtl range is relatively narrow. On the salt-side, the Prandtl number varies more significantly due primarily to its viscosity reduction and conductivity increase with increasing temperature.

Table 7
Heat transfer correlations from experimental data

Fluid *Geometry*	**Nusselt Number** **Colburn *J* factor**	**Operating Range**
Supercritical CO_2 *37° ZZ* *semi-elliptical*	$Nu = 0.0163\, Re^{0.922} Pr^{\frac{1}{3}}$ $j = 0.0163 * Re^{-0.078}$	Re = [5000, 40000] Pr = [0.733 - 0.777]
Solar Salt *30° ZZ elliptical*	$Nu = 0.412\, Re^{0.51} Pr^{\frac{1}{3}}$ $j = 0.412 * Re^{-0.49}$	Re = [100, 750] Pr = [3.4, 7.2]

Figure 13 shows the percentage error in predicted overall conductance (UA_{pred}) versus the average Reynolds number of the CO_2 and nitrate salt stream associated with each datapoint. This error is defined by equation 12 below, where the measured conductance (UA) of each data point is defined by equation 7. Positive error implies that the correlation overpredicts the heat transfer performance of the component.

$$UA\ Error\ [\%] = \frac{(UA_{pred} - UA)}{UA} \cdot 100\ [\%] \quad \textbf{[12]}$$

$$Nu_{Katz} = 0.0163\, Re^{0.922} Pr^{\frac{1}{3}} \quad \textbf{[13]}$$

Recall, the overall conductance is decomposed into three resistances, including the wall's conduction resistance and the convection resistance associated with each fluid (salt and CO_2). To assist the optimization of the salt-side correlation, the heat transfer correlation proposed by [10], shown in equation 13 was used as a starting point for the CO_2-side. This correlation in conjunction with the salt-correlation shown in Table 7 predicted the conductance to within ± 20%. Due to the lack of longitudinal fluid temperature measurements, the Reynolds and Prandtl number is determined using the linear average of the terminal fluid temperatures in this work. The correlation in equation 13 was created using an integrated average of four fluid temperatures for Reynolds/Prandtl calculation. Due to the slight difference in experimental technique, a new correlation shown in Table 7 was proposed for the CO_2-side. The new correlation suggested a Nusselt number 6.5% less than equation 13 at Reynolds of 5,000 and 3% greater at Reynolds of 40,000. Using the new CO_2 correlation and a finalized salt correlation also shown in Table 7, nearly all data with acceptable experimental uncertainty can be predicted to within ± 15%, as shown in Figure 13.

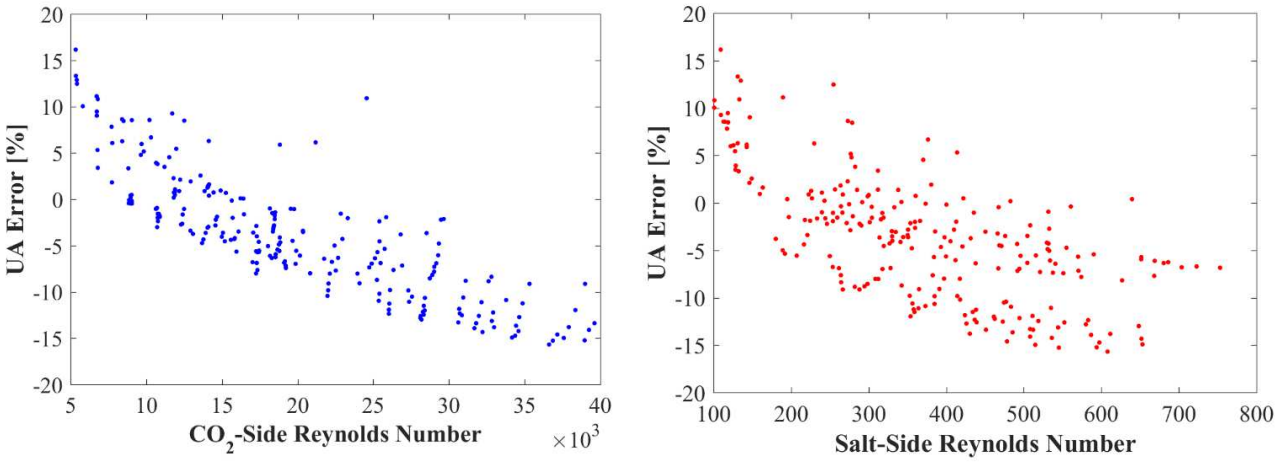

Figure 13. Error in calculated UA versus Salt-Side Reynolds number

The unresolved trend, observed clearly in the plot of CO_2 Reynolds versus percentage error is believed to be due to two effects. First, at low CO_2 flow rates the longitudinal temperature distribution in expected to become non-linear due to the capacitance ratio being significantly less than 1. Evaluation of the average Reynolds number becomes skewed and the heat transfer area participating in thermal exchange shrinks as the CO_2 temperature converges to the outlet temperature before the heat exchanger outlet. Second, axial conduction in the heat exchanger wall becomes significant when the stream capacitance ratio is small, or effectiveness is high [51]. While axial conduction is primarily driven by the thick walls of the DBHE, Solar

Salt, whose thermal conductivity (~0.5 W/m-K) is roughly 10 times greater than that of sCO_2, also contributes to axial conduction. Axial conduction degrades the thermal performance, especially when effectiveness is high, which is an inherent trait of a well-designed compact heat exchanger. Without additional information regarding the longitudinal temperature distribution, it was not possible to pursue this claim further.

In summary, the proposed correlations in Table 7 provide reasonably accurate estimates of the heat transfer performance (±15%) observed in this laboratory-scale heat exchanger. A simple non-discretized analysis method was employed, given the challenges of measuring the thermal performance of compact heat exchangers, such as inability to measure microchannel wall and bulk fluid temperatures within the core. The correlations in Table 7 show enhanced CO_2 convection behavior compared to Dittus-Boelter and close agreement with a previous helium-CO_2 experimental DBHE study [10]. The nitrate salt convection behavior shows significant enhancement compared to the analytical solution for straight circular channels under constant heat flux ($Nu = 4.36$) [46]. The enhanced heat transfer performance observed over a wide range of conditions and lack of operational issues during this novel use of molten salt in circular zig-zag microchannels emphasizes the need to pursue this technology further.

4.5. Quantification of heat losses

A heat loss test was also performed to bound the heat losses from the DBHE. The external heaters clamped to the exterior of the heat exchanger were used to bring the entirety of the heat exchanger above 560°C, the maximum operating temperature during heat transfer testing. Both the salt and CO_2 fluid passages were filled only with atmospheric air since both loops were empty and at ambient temperature during this test. Once all temperature measurements on or within the heat exchanger exceeded 560°C, the heaters were turned off and the component was allowed to equilibrate naturally with its surroundings. Three K-type thermocouples welded directly to the rear face of the DBHE were monitored for 12 hours after the heaters were turned off. Using the rate of temperature change, the known mass of the component (m), and the specific heat capacity of 316 stainless steel, the heat loss is estimated using equation 14. For simplicity, the specific heat of stainless steel is taken as the average value between 350-550°C which corresponds the salt operating temperature range in this work.

$$\dot{Q} = m\, C_P \frac{dT}{dt} = 7.5kg\, \left(0.512 \frac{J}{kg \cdot K}\right) \frac{dT}{dt} \quad \textbf{[14]}$$

Figure 14 shows the calculated heat loss versus the average temperature measured by the three external thermocouples. At 550°C, heat losses are around 180 W while at 350°C the heat losses are nearly half this value. Thermal imaging during testing revealed the hottest locations to be near the structural tabs which penetrate through the insulation. These tabs, shown in Figure 1 support the component in an upright orientation and accommodate thermal expansion but contribute significantly to heat loss. The electrical leads for the resistive heaters are expected to be another significant source of heat loss. The heaters were 0.5 mm Incoloy 800H shim stock laser-cut into a serpentine shape. Each heater was electrically isolated from the DBHE and the supporting structure by 0.75 mm mica sheet on either side of the heater. A 25-mm thick insulation board and stainless-steel plate compressed the mica sheets and heater against the flat surface of the heat exchanger to reduce the thermal contact resistance. Copper leads clamped onto 38 x 50 mm tabs on either end of the serpentine heater. A DC power supply provided up to 40 VDC across these serpentines, to produces slightly more the 1 kW heat input each. The copper leads are not thermally insulated to reduce the copper and power conductor temperature. The relative lack of insulation near these large heater tabs results in notable heat loss. However, the tabs are located at the end of the heat exchanger beyond the location of terminal fluid temperature measurements and are therefore not expected to significantly affect the heat transfer measurements. The hot- and cold-end temperatures in Figure 14 initially show lower heat loss when the heaters are turned off as the colder ends of the heat exchanger equilibrate with the center of the component. Once isothermal, all three external thermocouples cool at nearly the same rate.

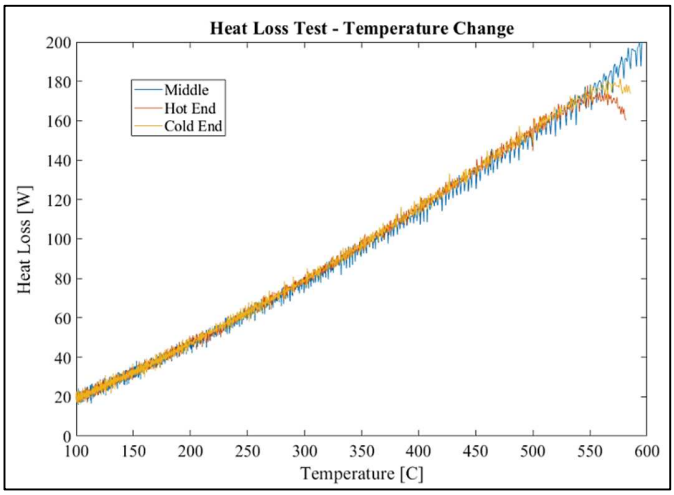

Figure 14. Heat loss from component versus core temperature

This environmental equilibration technique is considered conservative because the adjacent CO_2 and salt piping were not at the evaluated temperatures observed during heat transfer testing. The CO_2 nozzles especially constitute a significant conduction area due to the larger wall thickness required for pressure retainment. The salt-side pressure transducers, which are relatively large (~ 4 kg each), were also not heated during this test, resulting in additional heat losses via conduction along the salt-side pressure taps. The CO_2 side pressure taps were wrapped with ceramic wool 8 cm (3 in) beyond the heat exchanger insulation boundary to surround the fitting which transitioned to thinner, uninsulated tubing which remained below 40°C during testing. When both fluids are flowing through the heat exchanger, a temperature gradient of at least 50°C exists across the component, which safely bounds the heat losses below 180 W under all test conditions since only the hot end is near or below 550°C.

A complementary analysis of heat losses simply compares the heat duty of the nitrate salt and CO_2 streams. This was plotted for all data points in Figure 11. Nearly all data points exhibited heat duty for the salt and CO_2 streams within 10% of one another. Since nearly all data points exceeded 2 kW, 10% heat duty deviation bounds the ~ 200 W indicated by the heat loss analysis above. As mentioned in Section 4.3, other factors such as large venturi flow meter uncertainty and low temperature differential at low heat duty (< 5 kW) result in some points lying outside the 10% boundary. In lieu of correcting the overall conductance for heat loss, any data point with less than 3 kW heat transfer or greater 8% difference in stream heat duty was omitted from the analysis presented above.

5. Discussion

5.1. Prediction of non-isothermal pressure drop

While the friction factor correlations provided in Table 6 were generated using data collected under isothermal conditions, a component designer seeks to estimate the pressure drop during thermal exchange between the fluids. To examine the utility of the correlations provided in Table 6, these are used to estimate the pressure drop observed during heat transfer testing. Since a detailed analysis of header/transition regions of the heat exchanger was not possible, this discussion only addresses losses in the core region. Flow acceleration is considered using the inlet and outlet fluid temperatures to estimate the density change across the core. The difference between the pressure drop prediction including frictional losses in the zig-zag channels and flow acceleration, and the measured pressure drop during non-isothermal testing is presented in a percentage error.

Figure 15 shows the predictive error in the CO_2 – side pressure drop under non-isothermal conditions versus Reynolds number in the core region. Negative error implies underprediction by the proposed correlation shown in the plot for easy reference. The error bars associated with these data include the propagated measurement uncertainty of the Coriolis flowmeter, differential pressure across the heat exchanger, and the density change derived from terminal temperature measurements. Reynolds number uncertainty is smaller than the data markers due to the exceptional accuracy of the Coriolis flow meter and relative lack of viscosity temperature-dependence. Nearly all pressure-drop estimates lie within ±15% of the measured value. The friction factor correlation tends to underpredict pressure drops at low Reynolds number. The correlation is less accurate in this region due to erratic results during isothermal testing and proximity to the transition regime. The error bars shown, dominated by differential pressure error, support the claim that friction factor correlation can predict the core pressure losses to within ± 15% under most non-isothermal test conditions.

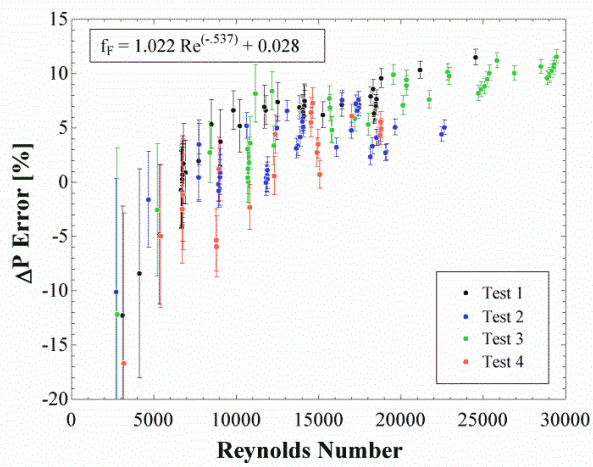

Figure 15. Prediction of non-isothermal CO_2 pressure drop using proposed correlation

Similarly, Figure 16 shows the error in core pressure drop prediction versus Reynolds number on the salt-side. The error bars associated with these data include measurement uncertainty associated with the venturi (discharge coefficient), differential pressure across the venturi and heat exchanger, and the density change derived from terminal temperature measurements. Reynolds number uncertainty encompasses only the variation in viscosity with temperature. The venturi flowmeter also plays a role, but this is neglected for the sake of visualizing the change in viscosity across the core. Several factors play into the larger deviation observed in this dataset. Large deviation in pressure drop prediction at low flow rates is due to high uncertainty in the differential pressure measurements and the potential for unequal flow distribution under low flow conditions. Most data below Reynolds of 200 was collected during the first salt tests when salt flow was limited by a partially clogged filter. For flow conditions near the design point (Re ~ 600), the friction factor correlation in Table 4 can predict the core pressure losses to within ± 15% under most non-isothermal test conditions. No data was collected during the fourth and final salt testing campaign due to the relocation of the differential pressure transducers to measure the overall pressure loss across the heat exchanger.

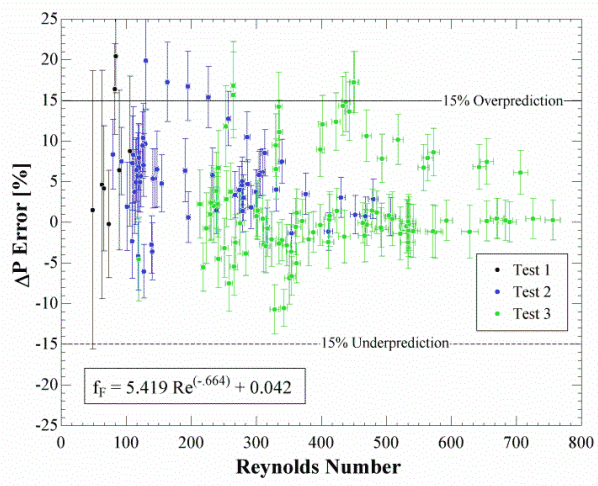

Figure 16. Prediction of non-isothermal salt pressure drop using proposed correlation

5.2. Freeze-thaw test results

During testing, the heat exchanger was subjected to several thermal transients resulting in ramp rates in the range of 1-5°C/s during rapid salt or CO_2 flow changes. Previous studies have shown DBHE respond very well to repeated, aggressive thermal transients [52] although this is an area needing further investigation, especially for nuclear-grade components to be commercialized. A common concern among compact heat exchanger developers is the effect of a freeze/thaw cycle, however no attempt to freeze molten salt in a DBHE has yet been published. To address this gap, a freeze test was performed prior to the final shutdown of the test facility. With the sCO_2 flow at approximately 0.14 kg/s (~50% of the maximum during heat transfer testing), an immediate stoppage of hot-side flow was achieved by closing one of the isolation valves on the NSL test

section. Maintaining the CO_2 flow results in a relatively rapid cold shock to the hot end of the heat exchanger, as shown in Figure 17. Without incoming salt, the heat exchanger converged to the CO_2 inlet temperature (~175°C). The external temperatures at the hot and cold-ends of the component were near the CO_2 headers, and therefore closely match the CO_2 fluid temperatures. Meanwhile, the external temperature at the middle of the heat exchanger shows a slow cooling trend caused by the initial freezing and thaw near the salt's melting point (220°C).

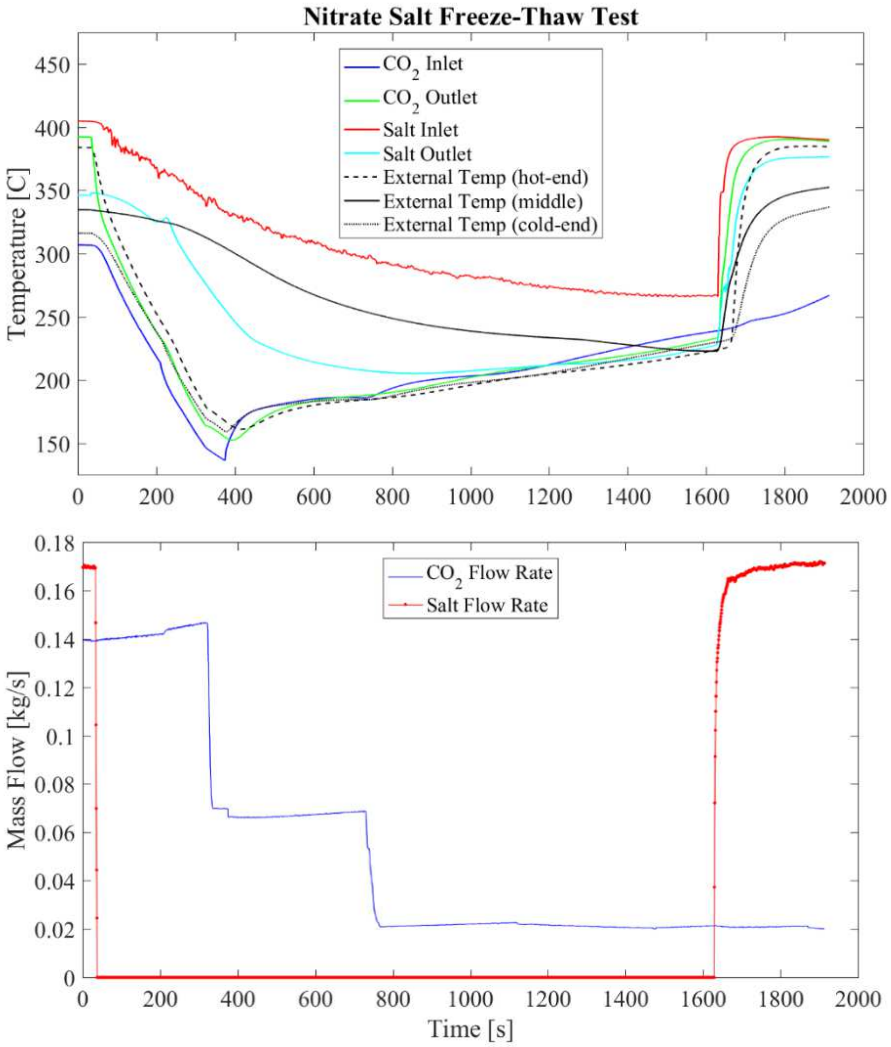

Figure 17. Temperature evolution (top) and flow rate (bottom) during salt freeze/thaw test

To accelerate the cooling of salt in the heat exchanger, the recuperator bypass fraction was increased from 10% to 25% until the CO_2 outlet temperature dropped below the salt's freezing temperature. Reopening the salt supply valve, located 5 meters upstream of the heat exchanger resulted in no flow response. Typically, flow would result in a rapid return of the salt inlet temperature to the loop's operating temperature complimented by the venturi flow meter signal. As the salt outlet temperature dropped below the freezing point, the CO_2 flow rate was reduced to 0.06 kg/s and ~ 300 seconds, and shortly after to 0.02 kg/s. The external heaters clamped to the heat exchanger were energized to provide ~ 3 kW of heat input. Meanwhile, two 1.2 kW tape heaters on the supply and return lines between the salt DBHE and the CO_2 recuperator were also energized. The tape heaters served to raise the temperatures of the CO_2 exiting the recuperator, and thus assisted in the melting process. After 20 minutes of heat input, the flow resumed suddenly, resulting in a rapid 180°C hot-shock over the course of the next 15 seconds. Upon thawing and returning to steady-state conditions, the CO_2 pump was stopped and another salt-side friction factor test was performed to confirm repeatable results. No significant difference between these results and the other friction factor data could be observed. X-ray examination of the heat exchanger after this test did not reveal any significant internal deformation of the microchannels.

Review of the temperature evolution shown in Figure 17 suggests that the salt-side heat exchanger did not freeze entirely. The middle, external temperature, and salt inlet heater remained near or above salt's melting temperature for the duration of the test. This implies that the salt was still liquid in the lower half of the heat exchanger. Intuitively, the salt freeze front started near the CO_2 inlet header (coldest location) and worked its way down the microchannels. As the heaters were energized, the CO_2 inlet temperature exceeded the outlet temperature to input heat into the component. This heat input may have caused a significant localized pressure near the salt outlet headers as the salt thawed and subsequently expanded. The authors expect the lack of a full freeze in the component was a significant contributor to the lack of observed damage. For commercial heat exchangers, it may be necessary to implement multiple heat zones to thaw the component from one end. The use of an auxiliary CO_2 heater upstream of the heat exchanger could potentially be used to thaw out the salt-side as this should provide a temperature distribution conducive to melting from an open end. In summary, this test provides some confidence that DBHE can be recovered from a partial salt freeze event and this discussion should be considered during future freeze-thaw tests, likely required for accident analyses.

5.3. Observations from post-test x-ray examination

After removal from the experimental test facility, the DBHE was examined in the Wisconsin x-ray tomography system under the same parameters as before high-temperature testing. The salt and CO_2-side process piping were cut using a wheeled pipe cutter to produce a clean break. After removal from the WisCO_2 – NSL test facility, the heat exchanger went directly into the x-ray system. 3-D computed tomography (CT) revealed very little salt remained in the heat exchanger core. Some residual frozen salt could be observed in the lower header, but no channels appeared to be blocked by frozen salt. One of the major concerns of using molten salt in a heat exchanger with small channels is the potential for plugging or fouling. Unfortunately, it was only possible to non-destructively examine the internals of the component once after testing. Water tests conducted between salt testing campaigns and after the x-ray examination produced results within 10% of each other in the first five data points, collected at the same flow rate conditions. This data suggests there were not any blocked passages and any residual salt which may have affected the water pressure loss measurement was quickly dissolved. The use of a relatively fine (400-micron) wire mesh filter is likely the cause of this promising observation.

Due to the presence of salt in the proprietary header regions, and lack of sharp contrast between the frozen salt and the heat exchanger headers or instrumentation ports, images of these deposit have not been included here. Future designs should implement sloped header walls to encourage residual salt to flow towards the bottom nozzle. A blow-down port at the top of the heat exchanger may also prove useful in the ability to blow out most of the residual salt with preheated air or superheated steam. Additional ports in the bottom header could also be useful for visual inspection via a borescope after shutdown or cleaning without removal from the process piping.

5.4. Recommendations for future work

This work examines a commercially-available, diffusion-bonded heat exchanger geometry using nitrate salt and supercritical CO_2. Salt filtration was one of the most challenging aspects of testing this component. Future researchers are encouraged to design a filter assembly which enables inspection and replacement of the filter screen when necessary. Given the acceptable performance of circular salt channels, future studies should consider the use of semi-circular channels to avoid manufacturing challenges associated with this geometry and the risk of plate misalignment due to inward-facing etched geometries. Even minor misalignment of the adjacent plates will significantly distort the stress distribution within the component. Minimal misalignment (~0.1 mm offset) was observed on one of the salt-side layers in the volumetric x-ray reconstruction. Hybrid designs utilizing formed fins on the liquid, low-pressure side may be a better option for more corrosive salts such as fluoride or chloride mixtures being investigated by nuclear or solar developers. Friction factor correlations proposed here for the semi-circular channels with water could be used to estimate salt pressure drop in this geometry, although they may be excessive for commercial applications.

Furthermore, investigation of a DBHE with external headers is highly recommended for two reasons. First, external headers can employ a simple and non-proprietary geometry which can be described in detail to complement thermal hydraulic performance results. Second, internal headers are inherently space-constrained which tends to increase fluid velocity and pressure drop. External headers could enable a straight-through flow path on the liquid-side that would provide useful operational insights for forced and natural circulation relevant to normal and abnormal operating conditions associated with a commercial power plant. Relatively low fluid velocity in the external headers may provide better flow distribution among the microchannels as well.

Finally, internal temperature measurements are invaluable to detailed thermal hydraulic studies. Recent work at the University of Wisconsin – Madison employed fiber optic temperature sensors to examine the wall temperature profile during a suite of steady-state DBHE tests with sCO_2 on both sides [53]. Studies seeking to evaluate assumptions regarding uniform flow distribution, header effects, and transient behavior should make used of distributed temperature sensors whenever

possible. Detailed understanding of the temperature distribution inside a compact heat exchanger is also crucial to detailed thermal-mechanical analyses required for high-temperature applications.

6. Conclusions

A 316/L stainless steel diffusion-bonded heat exchanger manufactured by Vacuum Process Engineering was tested at high-temperature between a Solar Salt (0.6 $NaNO_3$ – 0.4 KNO_3) loop and a supercritical CO_2 loop. To the authors' knowledge, this is the first DBHE designed with ASME Section VIII Code rules to be examined with molten salt. A modified definition of the hydraulic diameter, flow and heat transfer area is provided to facilitate comparison with recent and future zig-zag heat exchanger studies. The use of in-core pressure measurements and high-temperature pressure and flow instrumentation enabled collection of a large dataset of thermal hydraulic performance data for both fluids. A simple non-discretized analysis of this data led to the following correlations and conclusions:

1. Fanning friction factor correlations were proposed and used to estimate non-isothermal pressure drop observed during heat transfer testing. Independent hydraulic tests with water were conducted to compare the experimental friction factor trends. Water and salt friction factor correlations on the salt-side exhibits excellent agreement, emphasizing the utility of surrogate fluid experiments. Therefore, water tests on the CO_2 – side produce a friction correlation which could be used to estimate salt pressure losses in future heat exchangers exploring the use of semi-circular zig-zag channels.
2. Measurement of header pressure losses in this prototypic component provided a baseline for custom header designs and a rough estimate for these losses for similar pilot-scale components. Trade-offs between internal and external headers are discussed as this design choice may result in significant fixed and operational costs discrepancies at the commercial scale.
3. Colburn factor and Nusselt correlations for Solar (nitrate) Salt and supercritical CO_2 were proposed and shown to predict the heat exchanger performance under the experimental conditions within ±15%. Both correlations show enhanced heat transfer performance compared to those associated with straight channels and no significant fouling or operational issues were observed.
4. The use of a 400-micron wire mesh screen upstream of the heat exchanger removed entrained particulates and protected the heat exchanger from fouling or plugging with acceptable parasitic pressure losses. Design of a filter assembly which can be easily disassembled and cleaned should be employed by future users of molten salt compact heat exchangers.
5. Excellent draining performance was observed by a combination of x-ray examination and water pressure loss testing upon removal from the test facility. No plugged channels were observed, and only minimal salt deposits were discovered in the header ports and horizontally oriented instrumentation ports. Vertical orientation and use of headers with sloped edges to facilitate complete draining is suggested for future applications and the utility of auxiliary blow-down or inspection ports was discussed.
6. This lab-scale heat exchanger was shown to survive a partial freeze-thaw cycle with a continuous pressure of 10 MPa on the CO_2-side of the heat exchanger. Further testing is required to explore the possibility of recovering a component which has frozen solid on the salt-side. Damage from this abnormal event is expected to be highly dependent on the salt composition (chloride vs. nitrates, etc.) and geometry selection.

Declaration of interest

The authors declare there are no conflicts of interest in producing or publishing this work.

Acknowledgements

This material is based upon work supported by the Department of Energy Office of Nuclear Energy's Nuclear Energy University Program under Award Number DE-NE0008714. The authors would also like to extend special thanks to Vacuum Process Engineering for supplying the heat exchanger examined in this work and their permission to publish the performance data shown here.

constitute or imply its endorsement, recommendation, or favoring by the United States Government or any agency thereof. The views and opinions of authors expressed herein do not necessarily state or reflect those of the United States Government or any agency thereof.

References

[1] Sabharwall, P., Clark, D., Glazoff, M., Zheng, G., Sridharan, K., and Anderson, M., 2014, "Advanced Heat Exchanger Development for Molten Salts," Nuclear Engineering and Design, 280, pp. 42–56.

[2] Turchi, C., Gage, S., Martinek, J., Jape, S., Armijo, K., Coventry, J., Pye, J., Asselineau, C.-A., Venn, F., Logie, W., Fontalvo, A., Wang, S., McNaughton, R., Potter, D., Steinberg, T., and Will, G., 2021, *CSP Gen3: Liquid-Phase Pathway to SunShot*, NREL/TP--5700-79323, 1807668, MainId:33549.

[3] Klaus Brun, Peter Friedman, and Richard Dennis, eds., 2017, *Fundamentals and Applications of Supercritical Carbon Dioxide (SCO2) Based Power Cycles*, Woodhead Publishing, Cambridge, MA.

[4] Keating, R., Nestell, J., and McKillop, S., 2019, "Potential ASME Code Case for Compact Heat Exchangers in High Temperature Reactors," Tsukuba, Japan.

[5] Mahajan, H. P., Lima, L. M. A., and Hassan, T., 2021, "Mechanical and Microstructural Performance Evaluation of Diffusion Bonded Alloy 800H for Very High Temperature Nuclear Service," Journal of Engineering Materials and Technology, 144(2).

[6] Shaw, A., Jentz, I. W., Mahajan, H. P., and Hassan, T., 2020, "Assessment of Compact Heat Exchanger Design According to the Simplified ASME Analysis Methodologies," p. 11.

[7] Aakre, S. R., and Jentz, I. W., 2020, "Welded Attachments and Hydrostatic Pressure Testing Rules for Diffusion Bonded Heat Exchangers," *Pressure Vessels and Piping Conference*, American Society of Mechanical Engineers, p. V003T03A026.

[8] Shaw, A., Mahajan, H. P., and Hassan, T., 2020, "Assessment of Compact Heat Exchanger Design Following Elastic Perfectly Plastic Methodology," American Society of Mechanical Engineers Digital Collection.

[9] Selby, G., Aakre, S., and Fan, Z., 2020, "Non-Destructive Examination of Diffusion-Bonded Compact Heat Exchangers," *Pressure Vessels and Piping Conference*, American Society of Mechanical Engineers, p. V003T03A025.

[10] Katz, A., Aakre, S. R., Anderson, M. H., and Ranjan, D., 2021, "Experimental Investigation of Pressure Drop and Heat Transfer in High Temperature Supercritical CO2 and Helium in a Printed-Circuit Heat Exchanger," International Journal of Heat and Mass Transfer, 171, p. 121089.

[11] Che, S., Zhang, S., Burak, A., and Sun, X., 2021, "Structural Integrity Assessment of a Unit Cell in a Laboratory-Scale Printed Circuit Heat Exchanger for Molten Salt Reactors With Supercritical CO2 Power Cycle," *Volume 2: Computer Technology and Bolted Joints; Design and Analysis*, American Society of Mechanical Engineers, Virtual, Online, p. V002T03A014.

[12] ASME, 2015, "Section II, Part D: Material Properties (Metric)," *Boiler and Pressure Vessel Code*.

[13] 2012, "Companion Guide to the ASME Boiler and Pressure Vessel Code, Volume 2, Fourth Edition."

[14] Huang, C., Cai, W., Wang, Y., Liu, Y., Li, Q., and Li, B., 2019, "Review on the Characteristics of Flow and Heat Transfer in Printed Circuit Heat Exchangers," Applied Thermal Engineering, 153, pp. 190–205.

[15] Chai, L., and Tassou, S. A., 2020, "A Review of Printed Circuit Heat Exchangers for Helium and Supercritical CO2 Brayton Cycles," Thermal Science and Engineering Progress, 18, p. 100543.

[16] Yoon, S. H., No, H. C., and Kang, G. B., 2014, "Assessment of Straight, Zigzag, S-Shape, and Airfoil PCHEs for Intermediate Heat Exchangers of HTGRs and SFRs," Nuclear Engineering and Design, 270, pp. 334–343.

[17] Feher, E. G., 1968, "The Supercritical Thermodynamic Power Cycle," Energy Conversion, 8(2), pp. 85–90.

[18] Vaclav Dostal, 2004, "A Supercritical Carbon Dioxide Cycle for Next Generation Nuclear Reactors," PhD Thesis, Massachusetts Institute of Technology.

[19] Nikitin, K., Kato, Y., and Ngo, L., 2006, "Printed Circuit Heat Exchanger Thermal–Hydraulic Performance in Supercritical CO2 Experimental Loop," International Journal of Refrigeration, 29(5), pp. 807–814.

[20] Ngo, T. L., Kato, Y., Nikitin, K., and Ishizuka, T., 2007, "Heat Transfer and Pressure Drop Correlations of Microchannel Heat Exchangers with S-Shaped and Zigzag Fins for Carbon Dioxide Cycles," Experimental Thermal and Fluid Science, 32(2), pp. 560–570.

[21] Moisseytsev, A., Sienicki, J. J., Cho, D. H., and Thomasa, M. R., 2010, "Comparison of Heat Exchanger Modeling with Data from CO_2-to- CO_2 Printed Circuit Heat Exchanger Performance Tests," Proceedings of the 2010 International Congress on Advances in Nuclear Power Plants - ICAPP '10.

[22] Alan Michael Kruizenga, 2010, "Heat Transfer and Pressure Drop Measurements in Prototypic Heat Exchangers for the Supercritical Carbon Dioixde Brayton Power Cycles," PhD Thesis, University of Wisconsin - Madison.

[23] Baik, S., Kim, S. G., Lee, J., and Lee, J. I., 2017, "Study on CO2 – Water Printed Circuit Heat Exchanger Performance Operating under Various CO_2 Phases for S-CO_2 Power Cycle Application," Applied Thermal Engineering, 113, pp. 1536–1546.

[24] Lee, S.-M., and Kim, K.-Y., 2013, "Comparative Study on Performance of a Zigzag Printed Circuit Heat Exchanger with Various Channel Shapes and Configurations," Heat Mass Transfer, 49(7), pp. 1021–1028.
[25] Kim, S. G., Lee, Y., Ahn, Y., and Lee, J. I., 2016, "CFD Aided Approach to Design Printed Circuit Heat Exchangers for Supercritical CO2 Brayton Cycle Application," Annals of Nuclear Energy, 92, pp. 175–185.
[26] Meshram, A., Jaiswal, A. K., Khivsara, S. D., Ortega, J. D., Ho, C., Bapat, R., and Dutta, P., 2016, "Modeling and Analysis of a Printed Circuit Heat Exchanger for Supercritical CO2 Power Cycle Applications," Applied Thermal Engineering, 109, pp. 861–870.
[27] Scott, D., and Grindell, A. G., 1967, *Components and System Development for Molten-Salt Breeder Reactors*, ORNL-TM-1855, Oak Ridge National Laboratory.
[28] Britsch, K., and Anderson, M., 2020, "A Critical Review of Fluoride Salt Heat Transfer," Nuclear Technology, 206(11), pp. 1625–1641.
[29] Bin, L., Yu-ting, W., Chong-fang, M., Meng, Y., and Hang, G., 2009, "Turbulent Convective Heat Transfer with Molten Salt in a Circular Pipe," International Communications in Heat and Mass Transfer, 36(9), pp. 912–916.
[30] Carling, R., and Mar, R., 1981, *Industrial Use of Molten Nitrate/Nitrite Salts*, SAND-81-8020, 5257229, ON: DE82010032.
[31] González-Roubaud, E., Pérez-Osorio, D., and Prieto, C., 2017, "Review of Commercial Thermal Energy Storage in Concentrated Solar Power Plants: Steam vs. Molten Salts," Renewable and Sustainable Energy Reviews, 80, pp. 133–148.
[32] Dai, Z., Zheng, Z., Fletcher, D. F., and Haynes, B. S., 2015, "Experimental Study of Transient Behaviour of Laminar Flow in Zigzag Semi-Circular Microchannels," Experimental Thermal and Fluid Science, 68, pp. 644–651.
[33] Kim, I. H., Zhang, X., Christensen, R., and Sun, X., 2016, "Design Study and Cost Assessment of Straight, Zigzag, S-Shape, and OSF PCHEs for a FLiNaK–SCO2 Secondary Heat Exchanger in FHRs," Annals of Nuclear Energy, 94, pp. 129–137.
[34] Di Ronco, A., Cammi, A., and Lorenzi, S., 2020, "Preliminary Analysis and Design of the Heat Exchangers for the Molten Salt Fast Reactor," Nuclear Engineering and Technology, 52(1), pp. 51–58.
[35] Wang, W.-Q., Qiu, Y., He, Y.-L., and Shi, H.-Y., 2019, "Experimental Study on the Heat Transfer Performance of a Molten-Salt Printed Circuit Heat Exchanger with Airfoil Fins for Concentrating Solar Power," International Journal of Heat and Mass Transfer, 135, pp. 837–846.
[36] Fu, Q., Ding, J., Lao, J., Wang, W., and Lu, J., 2019, "Thermal-Hydraulic Performance of Printed Circuit Heat Exchanger with Supercritical Carbon Dioxide Airfoil Fin Passage and Molten Salt Straight Passage," Applied Energy, 247, pp. 594–604.
[37] Shi, H.-Y., Li, M.-J., Wang, W.-Q., Qiu, Y., and Tao, W.-Q., 2020, "Heat Transfer and Friction of Molten Salt and Supercritical CO2 Flowing in an Airfoil Channel of a Printed Circuit Heat Exchanger," International Journal of Heat and Mass Transfer, 150, p. 119006.
[38] Kim, I. H., and No, H. C., 2011, "Thermal Hydraulic Performance Analysis of a Printed Circuit Heat Exchanger Using a Helium–Water Test Loop and Numerical Simulations," Applied Thermal Engineering, 31(17), pp. 4064–4073.
[39] "Section VIII, Divsion 1, Appendix 13-9," *Boiler and Pressure Vessel Code*, Amercian Society of Mechanical Engineers.
[40] Jim Nestell and T.-L. Sham, 2015, *ASME Code Considerations for the Compact Heat Exchanger*, ORNL, Oak Ridge, TN.
[41] Aakre, S. R., Anderson, M. H., and Brooks, P. W., 2021, "Volumetric Efficiency and Pressure Pulsations of a Triplex Reciprocating Supercritical CO2 Pump," The Journal of Supercritical Fluids, 168, p. 105072.
[42] 14:00-17:00, "ISO/CD 5167-4," ISO [Online]. Available: https://www.iso.org/cms/render/live/en/sites/isoorg/contents/data/standard/07/91/79181.html. [Accessed: 01-Feb-2021].
[43] Reader-Harris, M., 2015, *Orifice Plates and Venturi Tubes*, Springer International Publishing.
[44] Pacheco, J. E., Ralph, M. E., Chavez, J. M., Dunkin, S. R., Rush, E. E., Ghanbari, C. M., and Matthews, M. W., 1995, *Results of Molten Salt Panel and Component Experiments for Solar Central Receivers: Cold Fill, Freeze/Thaw, Thermal Cycling and Shock, and Instrumentation Tests*, SAND-94-2525, Sandia National Lab. (SNL-NM), Albuquerque, NM (United States).
[45] Wagner, W., and Pruß, A., 2002, "The IAPWS Formulation 1995 for the Thermodynamic Properties of Ordinary Water Substance for General and Scientific Use," Journal of Physical and Chemical Reference Data, 31(2), pp. 387–535.
[46] Kays, W. M., and London, A. L., 1984, *Compact Heat Exchangers*, McGraw-Hill Inc., New York, New York.
[47] Span, R., and Wagner, W., 1996, "A New Equation of State for Carbon Dioxide Covering the Fluid Region from the Triple-Point Temperature to 1100 K at Pressures up to 800 MPa," Journal of Physical and Chemical Reference Data, 25(6), pp. 1509–1596.
[48] Lance, B. W., Carlson, M. D., Roberts, S. A., and Amogne, D., 2020, "Diffsusion Bonded Hydrogen Pre-Cooler Pressure Fatigue," *PVP2020-9267*, ASME, Minneapolis, MN, USA.

[49] Prieto, C., Ruiz-Cabañas, F. J., Rodríguez-Sanchez, A., Rubio Abujas, C., Fernández, A. I., Martínez, M., Oró, E., and Cabeza, L. F., 2019, "Effect of the Impurity Magnesium Nitrate in the Thermal Decomposition of the Solar Salt," Solar Energy, 192, pp. 186–192.
[50] Ho, C. Y., and Chu, T. K., 1977, *Electrical Resistivity and Thermal Conductivity of Nine Selected AISI Stainless Steels*, THERMOPHYSICAL AND ELECTRONIC PROPERTIES INFORMATION ANALYSIS CENTER LAFAYETTE IN.
[51] Kroeger, P. G., 1967, "Performance Deterioration in High Effectiveness Heat Exchangers Due to Axial Heat Conduction Effects," *Advances in Cryogenic Engineering*, K.D. Timmerhaus, ed., Springer US, Boston, MA, pp. 363–372.
[52] Pra, F., Tochon, P., Mauget, C., Fokkens, J., and Willemsen, S., 2008, "Promising Designs of Compact Heat Exchangers for Modular HTRs Using the Brayton Cycle," Nuclear Engineering and Design, 238(11), pp. 3160–3173.
[53] Jentz, I. W., and Anderson, M. H., 2020, "Coupled Heat Transfer and Hydraulic Modeling of an Experimental Printed Circuit Heat Exchanger Using Finite Element Methods," Journal of Thermal Science and Engineering Applications, 13(3).